

# CARBON-ENHANCED METAL-POOR STARS IN THE INNER AND OUTER HALO COMPONENTS OF THE MILKY WAY

DANIELA CAROLLO

Research School of Astronomy and Astrophysics, Australian National University, Cotter Road, Weston, ACT 2611, Australia  
INAF-Osservatorio Astronomico di Torino, Pino Torinese, Italy

TIMOTHY C. BEERS

Department of Physics & Astronomy and JINA: Joint Institute for Nuclear Astrophysics, Michigan State University,  
E. Lansing, MI 48824, USA

JO BOVY

Center for Cosmology and Particle Physics Department of Physics, New York University, 4 Washington Place, New York, NY 10003, USA

THIRUPATHI SIVARANI

Indian Institute of Astrophysics, II Block, Koramangala, Bangalore 560034, India

JOHN E. NORRIS, KEN C. FREEMAN

Research School of Astronomy and Astrophysics, Australian National University, Cotter Road, Weston, ACT 2611, Australia

WAKO AOKI

National Astronomical Observatory, Mitaka, Tokyo, 181-8588, Japan

YOUNG SUN LEE, CATHERINE R. KENNEDY

Department of Physics & Astronomy and JINA: Joint Institute for Nuclear Astrophysics, Michigan State University,  
E. Lansing, MI 48824, USA

## ABSTRACT

Carbon-enhanced metal-poor (CEMP) stars in the halo components of the Milky Way are explored, based on accurate determinations of the carbon-to-iron ( $[C/Fe]$ ) abundance ratios and kinematic quantities for over 30000 calibration stars from the Sloan Digital Sky Survey (SDSS). Using our present criterion that low-metallicity stars exhibiting  $[C/Fe]$  ratios (“carbonicity”) in excess of  $[C/Fe] = +0.7$  are considered CEMP stars, the global frequency of CEMP stars in the halo system for  $[Fe/H] < -1.5$  is 8%; for  $[Fe/H] < -2.0$  it is 12%; for  $[Fe/H] < -2.5$  it is 20%. We also confirm a significant increase in the level of carbon enrichment with declining metallicity, growing from  $\langle [C/Fe] \rangle \sim +1.0$  at  $[Fe/H] = -1.5$  to  $\langle [C/Fe] \rangle \sim +1.7$  at  $[Fe/H] = -2.7$ . The nature of the carbonicity distribution function (CarDF) changes dramatically with increasing distance above the Galactic plane,  $|Z|$ . For  $|Z| < 5$  kpc, relatively few CEMP stars are identified. For distances  $|Z| > 5$  kpc, the CarDF exhibits a strong tail towards high values, up to  $[C/Fe] > +3.0$ . We also find a clear increase in the CEMP frequency with  $|Z|$ . For stars with  $-2.0 < [Fe/H] < -1.5$ , the frequency grows from 5% at  $|Z| \sim 2$  kpc to 10% at  $|Z| \sim 10$  kpc. For stars with  $[Fe/H] < -2.0$ , the frequency grows from 8% at  $|Z| \sim 2$  kpc to 25% at  $|Z| \sim 10$  kpc. For stars with  $-2.0 < [Fe/H] < -1.5$ , the mean carbonicity is  $\langle [C/Fe] \rangle \sim +1.0$  for  $0 \text{ kpc} < |Z| < 10$  kpc, with little dependence on  $|Z|$ ; for  $[Fe/H] < -2.0$ ,  $\langle [C/Fe] \rangle \sim +1.5$ , again roughly independent of  $|Z|$ . Based on a statistical separation of the halo components in velocity space, we find evidence for a significant contrast in the frequency of CEMP stars between the inner- and outer-halo components – the outer halo possesses roughly twice the fraction of CEMP stars as the inner halo. The carbonicity distribution also differs between the inner-halo and outer-halo components – the inner halo has a greater portion of stars with modest carbon enhancement ( $[C/Fe] \sim +0.5$ ); the outer halo has a greater portion of stars with large enhancements ( $[C/Fe] \sim +2.0$ ), although considerable overlap still exists. We interpret these results as due to the possible presence of additional astrophysical sources of carbon production associated with outer-halo stars, beyond the asymptotic giant-branch source that may dominate for inner-halo stars, with implications for the progenitors of these populations.

*Subject headings:* Galaxy: Evolution, Galaxy: Formation, Galaxy: Halo, Galaxy: Structure, Methods: Data Analysis, Stars: Abundances, Surveys

## 1. INTRODUCTION

The Milky Way provides astronomers with a unique opportunity to explore the formation and evolution of large spiral galaxies, as well as the nature of their stellar populations and recognized structures. The key to this understanding comes from the availability, for large numbers of individual stars, of the powerful combination of six-dimensional phase-space information (location and velocity) and chemical abundances. Metal-poor stars, in particular, shed light on the early stages of galaxy formation and chemical evolution, as they represent the fossil record of the first generations of stars that formed shortly after the Big Bang.

Although theory suggests that the bulge of the Galaxy may harbor numerous ancient (though not necessarily the most metal-poor) stars (e.g., Tumlinson 2010), the vast majority of presently recognized metal-poor stars are found in the halo system of the Galaxy. According to Carollo et al. (2007; C07) and Carollo et al. (2010; C10), the inner and outer halos possess different peak metallicities ( $[\text{Fe}/\text{H}]_{\text{inner}} \sim -1.6$ ;  $[\text{Fe}/\text{H}]_{\text{outer}} \sim -2.2$ ), as well as different spatial distributions, with the inner halo exhibiting a flatter density profile than the nearly spherical outer halo. Their analysis of the kinematics of a local sample of calibration stars from the Sloan Digital Sky Survey (SDSS; York et al. 2000; Gunn et al. 2006) indicated that the transition from dominance by the inner halo to the outer halo occurs in the range 15–20 kpc from the Sun. A similar transition range has been inferred from analysis of the “vertical” photometric stripes (de Jong et al. 2010), obtained during the Sloan Extension for Galactic Understanding and Exploration (SEGUE) sub-survey of SDSS-II (Yanny et al. 2009).

The papers by C07 and C10 also demonstrated that the inner-halo population is essentially non-rotating, with  $V_\phi = 7 \pm 4 \text{ km s}^{-1}$ , while the outer-halo population exhibits a significant retrograde signature, with  $V_\phi = -80 \pm 13 \text{ km s}^{-1}$  (where  $V_\phi$  is the Galactocentric rotational velocity). The velocity ellipsoids of these populations differ as well, such that  $(\sigma_{V_R}, \sigma_{V_\phi}, \sigma_{V_z}) = (150 \pm 2, 95 \pm 2, 85 \pm 1) \text{ km s}^{-1}$  for the inner halo and  $(159 \pm 4, 165 \pm 9, 116 \pm 3) \text{ km s}^{-1}$  for the outer halo, evaluated in a Galactocentric cylindrical reference frame.

The observed differences in the nature of the spatial distributions and kinematics of the stellar populations associated with the inner- and outer-halo components suggests that, in the context of modern hierarchical cosmogonies, their progenitor mini-halos and subsequent merging and accretion scenarios differed as well. If the inner halo formed from a limited number of moderately massive mini-halos (see, e.g., Bullock & Johnston 2005; Schlaufman et al. 2009, 2011), while the outer halo resulted from the accretion of more numerous, but less massive ones (C07; Frebel et al. 2010; Norris et al. 2010a,b,c), one might expect to find chemical signatures associated with the presently observed stellar populations that reflect these differences. Previous studies have provided hints that this may indeed be the case. For example, studies of the  $[\text{Mg}/\text{Fe}]$  abundance ratios of stars thought to be associated with the inner halo appear different (generally 0.1 dex higher) than those associated with the outer halo (Roederer 2009). This same study also demonstrated that stars associated with the inner halo exhibit considerably lower star-to-star

abundance scatter for both the iron-peak element ratio  $[\text{Ni}/\text{Fe}]$  and the neutron-capture element ratio  $[\text{Ba}/\text{Fe}]$  than found for stars of the outer halo. The recent study by Nissen & Schuster (2010) demonstrated that nearby dwarfs with halo kinematics could be separated into two groups based on  $[\alpha/\text{Fe}]$ . They proposed that the high- $\alpha$  stars may have been born in the disk or bulge of the Milky Way and heated to halo kinematics by merging satellite galaxies, or else were simply members of the early generations of halo stars born during the collapse of a proto-Galactic gas cloud, while the low- $\alpha$  stars may have been accreted from dwarf galaxies. Schlaufman et al. (2009) report detections of numerous elements of cold halo substructure (ECHOS) in the inner halo, essentially overdensities in radial-velocity space along the SEGUE sightlines. The ECHOS are systematically more Fe-rich, but less  $\alpha$ -enhanced than the kinematically smooth component of the inner halo. The ECHOS are also chemically distinct from other Milky Way components; they are more Fe-poor than typical thick-disk stars, and both more Fe-poor and  $\alpha$ -enhanced than typical thin-disk stars. See Schlaufman et al. (2011) for a more detailed discussion.

Chemically peculiar stars, such as the  $\alpha$ -element-enhanced very metal-poor star BS 16934-002 (Aoki et al. 2007a;  $[\text{Fe}/\text{H}] = -2.7$ ), the low  $[\text{Mg}/\text{Fe}]$  ( $-0.1$ ), high  $[\text{Ca}/\text{Fe}]$  ( $+1.1$ ) extremely metal-poor star SDSS J2347+0108 (Lai et al. 2009;  $[\text{Fe}/\text{H}] = -3.2$ ), and the low  $[\text{Si}/\text{Fe}]$  ( $-1.0$ ), low  $[\text{Ca}/\text{Fe}]$  ( $-0.6$ ) extremely metal-poor star HE 1424-0241, identified by Cohen et al. (2007;  $[\text{Fe}/\text{H}] \sim -4.0$ ), all have inferred distances (and metallicities) that suggest membership in the outer-halo population. All three of the previously recognized ultra metal-poor stars ( $[\text{Fe}/\text{H}] \leq -4.0$ , HE 0557-4840; Norris et al. 2007) or hyper metal-poor stars ( $[\text{Fe}/\text{H}] \leq -5.0$ , HE 0107-5240; Christlieb et al. 2002, and HE 1327-2326; Frebel et al. 2005) are similarly thought to be members of the outer-halo population. Likewise, the newly discovered hyper metal-poor star SDSS J102915+172927 appears to have an orbit consistent with outer-halo membership (Caffau et al. 2011). These results may all be related to the star formation histories in the progenitor populations, their accretion histories, or both.

In the present paper we focus on another possibly useful indicator of chemical differences between the inner- and outer-halo components, the carbon-to-iron ratio,  $[\text{C}/\text{Fe}]$ , which we refer to as the “carbonicity.” In particular, we make use of the SDSS/SEGUE calibration-star sample from SDSS DR7 (Abazajian et al. 2009) in order to search for possible contrasts between the frequency and degree of carbon enhancement for the carbon-enhanced metal-poor (CEMP) stars from this sample that can be kinematically associated with these two halo components.

The CEMP stars were originally defined as the subset of very metal-poor stars ( $[\text{Fe}/\text{H}] \leq -2$ ) that exhibit elevated carbon relative to iron,  $[\text{C}/\text{Fe}] > +1.0$  (Beers & Christlieb, 2005)<sup>1</sup>. In the last two decades it has been recognized, primarily from spectroscopic follow-up of metal-poor candidates selected from objective-prism surveys (e.g., Beers et al. 1985, 1992; Christlieb 2003), that roughly 20% of stars with  $[\text{Fe}/\text{H}] < -2.0$  exhibit enhanced carbonicity, up to several orders of magnitude larger than the solar ratio (Marsteller et al. 2005; Lucatello et al. 2006). Some recent studies (e.g., Cohen et al. 2005; Frebel et al. 2006), have claimed that this fraction is a little lower (14% and 9%, respectively, for  $[\text{Fe}/\text{H}] < -2.0$ ).

Electronic address: aoki.wako@nao.ac.jp  
Electronic address: lee@pa.msu.edu; kenne257@msu.edu

<sup>1</sup> Other authors have used slightly different criteria, e.g.,  $[\text{C}/\text{Fe}] > +0.7$  (Aoki et al. 2007b).

The Frebel et al. (2006) study is of particular interest, as the authors argued that the relative fraction of CEMP stars appears to increase substantially with distance above the Galactic plane, suggesting a possible connection with changes in the underlying stellar populations. In any case, the fraction of CEMP stars rises to 30% for  $[\text{Fe}/\text{H}] < -3.0$ , 40% for  $[\text{Fe}/\text{H}] < -3.5$ , and 75% for  $[\text{Fe}/\text{H}] < -4.0$  (Beers & Christlieb 2005; Frebel et al. 2005; Norris et al. 2007; Caffau et al. 2011 – the new  $[\text{Fe}/\text{H}] = -5.0$  star does not exhibit carbon enhancement); definitive explanations for the origin of this increase have yet to be offered. Regardless of the ultimate reason, these results indicate that significant amounts of carbon were produced in the early stages of chemical evolution in the universe.

There exist a number of classes of CEMP stars, some of which have been associated with proposed progenitor objects. The CEMP-s stars (those with  $s$ -process-element enhancement), for example, are the most commonly observed type to date. High-resolution spectroscopic studies have revealed that around 80% of CEMP stars exhibit  $s$ -process-element enhancement (Aoki et al. 2007b). The favored mechanism invoked to account for these stars is mass transfer of carbon-enhanced material from the envelope of an asymptotic giant-branch (AGB) star to its binary companion; it is this surviving companion that is now observed as a CEMP-s star (e.g., Herwig 2005; Sneden et al. 2008; Bisterzo et al. 2011).

The class of CEMP-no stars (which exhibit no strong neutron-capture-element enhancements) is particularly prevalent among the lowest metallicity stars ( $[\text{Fe}/\text{H}] < -2.5$ ; Beers & Christlieb 2005; Aoki et al. 2007b). Possible progenitors for this class include massive, rapidly rotating, mega metal-poor ( $[\text{Fe}/\text{H}] < -6.0$ ) stars, which models suggest have greatly enhanced abundances of CNO due to distinctive internal burning and mixing episodes, followed by strong mass loss (Hirschi et al. 2006; Meynet et al. 2006, 2010a,b). Another suggested mechanism for the production of the material incorporated into CEMP-no stars is pollution of the interstellar medium by so-called faint supernovae associated with the first generations of stars, which experience extensive mixing and fallback during their explosions (Umeda & Nomoto 2003, 2005; Tominaga et al. 2007). This model well reproduces the observed abundance pattern of the CEMP-no star BD+44°493, the ninth-magnitude  $[\text{Fe}/\text{H}] = -3.7$  star (with  $[\text{C}/\text{Fe}] = +1.3$ ,  $[\text{N}/\text{Fe}] = +0.3$ ,  $[\text{O}/\text{Fe}] = +1.6$ ) discussed by Ito et al. (2009). The recently reported high redshift ( $z = 2.3$ ), extremely metal-poor Damped Lyman- $\alpha$  (DLA) system by Cooke et al. (2011;  $[\text{Fe}/\text{H}] \sim -3.0$ ) exhibits enhanced carbonicity ( $[\text{C}/\text{Fe}] = +1.5$ ) and other elemental abundance signatures that Kobayashi et al. (2011) also associate with production by faint supernovae. It is also of interest that Matsuoka et al. (2011) have reported evidence for strong carbon production in the early universe, based on their analysis of the optical spectrum of the most distant known radio galaxy, TN J0924-2201, with  $z = 5.19$ .

Below we seek to test if the increasing frequency of CEMP stars with declining metallicity, and the suggested increase of the fraction of CEMP stars with increasing distance from the Galactic plane, can be explained in the context of an inner/outer halo dichotomy and the dominance of *different carbon-production mechanisms* (the processes associated with the progenitors of the CEMP-s and CEMP-no stars) being linked to these two populations.

This paper is outlined as follows. Section 2 describes the techniques used to estimate the atmospheric parameters ( $T_{\text{eff}}$ ,  $\log g$ , and  $[\text{Fe}/\text{H}]$ ) and carbonicity ( $[\text{C}/\text{Fe}]$ ) from the low-resolution SDSS spectra, compares our estimates with a sam-

ple of very low-metallicity stars with available high-resolution spectroscopic determinations, and obtains first-pass estimates of the fractions of CEMP stars for various cuts on  $[\text{Fe}/\text{H}]$ . Section 3 summarizes the calibration-star sample from SDSS DR7 we examine here, presents the “as-observed” distributions of metallicity and carbonicity for this sample as functions of height above the Galactic plane, and carries out a comparison of the distance and rotational velocity distributions for CEMP and non-CEMP stars. Section 4 explores the global fraction of CEMP stars of this sample in the low-metallicity regime, describes our adopted technique for derivation of stellar population membership probabilities for the SDSS/SEGUE DR7 calibration stars, and obtains estimates of the fractions of CEMP stars associated with the inner- and outer-halo populations. Finally, Section 5 summarizes our main results and considers their implications for the formation and evolution of the Galactic halo populations.

## 2. ATMOSPHERIC PARAMETER ESTIMATES AND $[\text{C}/\text{Fe}]$ RATIOS FOR THE SDSS/SEGUE DR7 CALIBRATION-STAR SAMPLE

### 2.1. Atmospheric Parameter Estimates

Estimates of the atmospheric parameters for our program stars were obtained from the SEGUE Stellar Parameter Pipeline (SSPP papers I-V: Lee et al 2008a,b; Allende Prieto et al. 2008; Smolinski et al. 2011; Lee et al. 2011). Typical internal errors for stars in the temperature range that applies to the majority of the calibration-star sample are  $\sigma(T_{\text{eff}}) \sim 125$  K,  $\sigma(\log g) \sim 0.25$  dex, and  $\sigma([\text{Fe}/\text{H}]) \sim 0.20$  dex. The external errors in these determinations are of similar size, as discussed in the SSPP references listed above.

In C10, a correction was applied for the metallicity determinations of the SSPP, which we adopt here as well:

$$[\text{Fe}/\text{H}]_C = -0.186 + 0.765 * [\text{Fe}/\text{H}]_A - 0.068 * [\text{Fe}/\text{H}]_A^2 \quad (1)$$

where  $[\text{Fe}/\text{H}]_A$  is the adopted metallicity from the SSPP, and  $[\text{Fe}/\text{H}]_C$  is the corrected metallicity. This polynomial has little effect on stars with metallicity greater than about  $[\text{Fe}/\text{H}] = -2.5$ , but lowers the estimated metallicities for stars below this abundance by 0.1 to 0.2 dex, an offset that was shown to exist between the DR7 SSPP-derived metallicities and previous high-resolution spectroscopic measurements.

### 2.2. Estimation of Carbon Abundance Ratios

Carbon-to-iron abundance ratios ( $[\text{C}/\text{Fe}]$ ) are estimated from the CH G-band at  $\sim 4300$  Å by matching the observed SDSS spectra near this feature with an extensive grid of synthetic spectra. In order to construct the grid we employed the NEWODF models of Castelli & Kurucz (2003). Synthetic spectra were generated using the *turbospectrum* synthesis code (Alvarez & Plez 1998), which employs line broadening according to the prescription of Barklem & O’Mara (1998) and Barklem & Aspelund-Johansson (2005). The molecular species CH and CN are provided by B. Plez (private communication; Plez & Cohen 2005). The other linelists used are the same as in Sivarani et al. (2006). For the purpose of this exercise we adopted the solar abundances of Asplund et al. (2005).

The synthetic spectra cover wavelengths between 3600 Å and 4600 Å, with original resolution of  $\Delta\lambda = 0.005$  Å,



smoothed to the SDSS resolving power ( $R = 2000$ ) and rebinned to linear  $1\text{\AA}$  pixels. The stellar parameters of the grid cover the ranges  $3500\text{ K} \leq T_{\text{eff}} \leq 9750\text{ K}$  (steps of  $250\text{ K}$ ),  $0.0 \leq \log g \leq 5.0$  (steps of  $0.5\text{ dex}$ ) and  $-2.5 \leq [\text{Fe}/\text{H}] \leq 0.0$  (steps of  $0.5\text{ dex}$ ). For stars with  $[\text{Fe}/\text{H}] < -2.5$ , models with  $[\text{Fe}/\text{H}] = -2.5$  were adopted. At the time this analysis was carried out, lower metallicity models from this grid were not available. However, we did have sparsely-spaced carbon-enhanced models generated by B.Plez, which extended down to  $[\text{Fe}/\text{H}] = -5.0$ , for  $4000\text{ K} \leq T_{\text{eff}} \leq 6000\text{ K}$ . We carried out a number of tests of our use of the  $[\text{Fe}/\text{H}] = -2.5$  models extrapolated to lower metallicities, which produced results in good agreement with Plez’s models. Our program stars include objects with temperatures above  $6000\text{ K}$ , where any effects due to extrapolation to lower metallicities will be lower still. Indeed Masseron et al. (2005) points out that models with  $T_{\text{eff}} > 6000\text{ K}$  are not affected by enhanced carbon. In any event, our past experience using models of lower metallicity from other sources has indicated that very little changes when dropping below  $[\text{Fe}/\text{H}] = -2.5$ . This is also indicated by the generally excellent agreement of our  $[\text{C}/\text{Fe}]$  determinations with the high-resolution results discussed below. The carbon abundance in the grid goes from  $[\text{C}/\text{H}] = [\text{Fe}/\text{H}] - 0.5$  to  $[\text{C}/\text{H}] = +0.5$  (the upper limit is in agreement with AGB models). For example, at  $[\text{Fe}/\text{H}] = -2.5$ , the grid covers the range from  $[\text{C}/\text{H}] = -3.0$  to  $+0.5$ , which corresponds to the range of carbonicity  $-0.5 < [\text{C}/\text{Fe}] < +3.0$ .

Once constructed, we linearly interpolate within this grid, which is sufficient for the size of the steps in the parameters. We have checked this by taking a worst-case scenario, generating test synthetic spectra at low temperatures ( $T_{\text{eff}} = 3500\text{ K}$ ) and over the above ranges of gravity, metallicity, and carbon abundance. The linearly interpolated grid was able to recover the input parameters to within a few tenths of dex, which is consistent with our expected errors in the method. Estimation of carbon abundance was accomplished using chi-square minimization of the deviations between the observed and synthetic spectra in the wavelength region between  $4285\text{ \AA}$  and  $4320\text{ \AA}$ , as carried out by the IDL routine AMOEBA (a downhill Simplex search procedure). The initial value for  $[\text{C}/\text{H}]$  for the the global grid search was set to the same value as the input stellar  $[\text{Fe}/\text{H}]$  ( $[\text{C}/\text{Fe}] = 0.0$ ). During the search, the carbon abundances are allowed to vary; all other stellar parameters are kept constant. In order to provide some protection from falling into local minima, separate searches were performed with lower and higher ranges of  $[\text{C}/\text{Fe}]$  considered. In almost all cases these converged to the same minima as found for the global search. When not, we took the value that resulted in the best match in the region of the CH G-band, as judged from a correlation coefficient for the resulting match.

Figure 1 provides an example of the spectral matching process for determination of  $[\text{C}/\text{Fe}]$  for a warm CEMP star in our sample. The upper panel shows the input optical spectrum (black line) superposed with a synthetic spectrum with  $[\text{C}/\text{Fe}] = 0$  (red line). The middle panel shows the best matches to the CH G-band obtained from the three different ranges of  $[\text{C}/\text{Fe}]$  considered. The lower panel shows the final adopted match.

Note that our procedures are not traditional synthesis analyses, but are based on spectral matching. As part of this approach, the continuum-flattened observed spectra must be registered to match similarly flattened synthetic spectra. Because rectification of the stellar (and synthetic) continua is sometimes imperfect, small deviations over localized regions

of spectral range can occasionally appear. Careful inspection of the bottom panel of Figure 1 reveals, for example, a slight mismatch near the red end. We have taken care to minimize the occurrence of these mismatches to the extent feasible, with particular effort made in the range that is explored for performing the match to the CH G-band. In any case, since the atmospheric parameters are set before conducting the matching, slight registration offsets outside of the CH G-band region have no effect on our derived  $[\text{C}/\text{Fe}]$ . We note that most of the weak features in the region of the CH G-band are real, and not due to noise.

Similar procedures have been employed in previously published papers (Beers et al. 2007; Kennedy et al. 2011), to which we refer the reader for additional discussion of these techniques. We have also pursued a modest sanity check by carrying out full syntheses for a small number of spectra using the approach employed by Norris et al. (2010c), based on the synthesis code of Cottrell & Norris (1978). These comparisons indicate that we are able to replicate derived  $[\text{C}/\text{Fe}]$  by our spectral matching approach to within  $0.1\text{--}0.2\text{ dex}$ , at the one-sigma level in the precision for the majority of our program stars.

Estimates of the errors in the final determinations of  $[\text{C}/\text{Fe}]$  were obtained based on a set of noise-injection experiments for stars over a range of temperatures and S/N ratios. These experiments indicated that, for stars with a minimum  $\text{S/N} = 15/1$  in the region of the G-band,  $[\text{C}/\text{Fe}]$  could be measured over the  $T_{\text{eff}}$  range of our sample with a maximum error of  $0.5\text{ dex}$ , decreasing to  $0.05\text{ dex}$  for the highest S/N spectra ( $\text{S/N} > 50/1$ ). We assigned final errors to the estimate of  $[\text{C}/\text{Fe}]$  using a linear function in S/N between these extremes. Spectra not achieving the minimum S/N level (or which suffered from anomalies such as pixel dropouts) were considered non-observations (i.e., they were dropped from the sample). In addition, in order to claim a detection we required that the equivalent width of the CH G-band obtain a minimum value of  $1.2\text{ \AA}$ , a value again chosen based on inspection of the noise-injection experiments.<sup>2</sup> In cases where this condition was not met, we consider the measured  $[\text{C}/\text{Fe}]$  an upper limit.

### 2.3. Comparison with High-Resolution Spectroscopic Estimates

We obtain a check on our determinations of atmospheric parameters and  $[\text{C}/\text{Fe}]$ , for at least a subset of our stars, based on available high-resolution follow-up spectra. There are three sources for our comparisons: Aoki et al. (2008), Behara et al. (2010), and Aoki et al. (2011, in prep.). Since these high-resolution spectroscopic programs were mostly interested in very and extremely metal-poor stars, our comparison sample is dominated by stars with  $[\text{Fe}/\text{H}] < -2.5$ . Table 1 lists the derived atmospheric parameters and carbon abundance ratios for the stars in common (the label HIGH indicates the high-resolution results, while the label SSPP refers to our analysis of the low-resolution SDSS spectra). There are 23 unique objects listed, although one star has only upper limits for  $[\text{C}/\text{Fe}]$  determined. Note that four stars in this table were reported on by two sets of authors, which provides some feeling for the

<sup>2</sup> The CH G-band equivalent width measured in this study covers a wider wavelength region than that defined by Beers et al. (1999):  $26\text{ \AA}$  (this paper) vs.  $15\text{ \AA}$  (Beers et al. 1999), but centered on the same wavelength ( $4305\text{ \AA}$ ). It also makes use of a global fit to the continuum, rather than the fixed sidebands employed previously. Thus, although the equivalent widths are similar, they are not identical.



level of systematic differences in the derived parameters. The Aoki et al. (2011) paper, which supplies information for most of our comparison sample, concluded that the temperature estimates provided by the SSPP were sufficiently good that they simply adopted them for their analysis (although they tested alternative methods, they could not improve upon the SSPP results). As a result, a comparison of  $T_{\text{eff}}$  determinations for the high-resolution and low-resolution spectroscopic analyses cannot be fairly carried out. In the case of stars that were observed by multiple groups, straight averages of the listed parameters are used (except when the Aoki et al. 2011 *assigned* value of  $\log g = +4.0$ , as described below, can be replaced by a *measured* value from the other sources).

Figure 2 shows a comparison of the derived parameter estimates. Robust estimates of the zero-point offsets and rms scatter indicate good agreement in metallicity ( $\langle \Delta[\text{Fe}/\text{H}] \rangle = -0.09$  dex;  $\sigma([\text{Fe}/\text{H}]) = 0.27$  dex), close to the random errors expected for carbon-normal stars from the SSPP (0.2 dex). Surface gravity exhibits an acceptably small zero-point offset but a larger scatter ( $\langle \Delta(\log g) \rangle = -0.27$  dex;  $\sigma(\log g) = 0.66$  dex). Larger differences in the  $\log g$  determinations might be expected for several reasons. First, the comparison spectra for the majority of our program stars (18 of 23) are based, at least in part, on “snapshot” high-resolution spectra (i.e., lower S/N) spectra reported by Aoki et al. (2011). For these spectra, estimates of  $\log g$  were fixed to  $\log g = 4.0$  for all stars with  $T_{\text{eff}} > 5500$  K. This was done because the usual procedure of matching Fe abundances based on Fe I and Fe II lines was not uniformly possible for the warmer stars, due to the weakness of the Fe II lines and the less than ideal S/N. According to Aoki et al. (2011), the true surface gravities for such stars could lie anywhere in the range  $\log g = 3.5$  to  $\log g = 4.5$ . Note that the reported surface-gravity offset and scatter above does not include the three Aoki et al. (2011) stars that did not have reported estimates from other sources.

Surface gravity estimates from the high-resolution spectra of giants with  $T_{\text{eff}} < 5500$  K are determined by Aoki et al. (2011) based on analysis of the Fe I and Fe II lines, in the usual manner. Note that Aoki et al. also identified four stars in this temperature range to be cool main-sequence stars, rather than giants, based on the weak lines of their ionized species. For these stars, gravity estimates are obtained by matching to isochrones for metal-poor main-sequence stars (a similar process to that carried out by Aoki et al. 2010).

It is expected that the high-resolution analysis estimates of  $\log g$  for the cooler stars are precise at a level no better than 0.3 dex. Secondly, difficulty in estimation of  $\log g$  for CEMP stars might not be surprising, given that molecular carbon bands (in particular for later type stars) can easily confound gravity-sensitive features in a low-resolution spectrum. However, in our analysis we have taken care to avoid regions of the spectrum where molecular carbon bands have corrupted the gravity-sensitive features. In reality, this problem is only encountered for the coolest stars with the strongest molecular bands, which are a distinct minority of our sample. Our sample only includes stars in the temperature range  $4500 \text{ K} < T_{\text{eff}} < 7000 \text{ K}$ , and among the 813 carbon-rich stars considered in our analysis below, none of them have  $T_{\text{eff}} < 5000 \text{ K}$ , and only 10% have  $T_{\text{eff}} < 5750 \text{ K}$ . Taking a global approximation that the high-resolution determinations of surface gravity contribute 0.4 dex to the rms scatter comparison with the low-resolution estimates, this indicates that the SSPP estimates for these stars have an external error of determination of  $\sqrt{(0.66^2 - 0.4^2)} = 0.52$  dex. We also note that the

great majority of the stars analysed in our sample have  $[\text{Fe}/\text{H}] > -2.5$ , for which surface gravity estimates should be better determined, due to the increasing strength of their gravity-sensitive metallic features.

The agreement in estimates of the carbonicity is quite good ( $\langle \Delta[\text{C}/\text{Fe}] \rangle = +0.05$  dex;  $\sigma([\text{C}/\text{Fe}]) = 0.29$  dex), since we expect even the high-resolution determinations to be precise to no better than about 0.15-0.20 dex. This suggests that our external errors for estimates of  $[\text{C}/\text{Fe}]$  are on the order of 0.25 dex. Note that this level of agreement between  $[\text{C}/\text{Fe}]$  determinations based on the high-resolution and SSPP analyses would not be possible if the rough estimates of  $\log g$  had a strong influence on our procedures. However, at the suggestion of an anonymous referee, we have carried out explicit tests of the effect of incorrect surface-gravity determinations on the derived  $[\text{C}/\text{Fe}]$ .

In order to test the impact on the derived  $[\text{C}/\text{Fe}]$  from the adoption of an incorrect surface gravity, we have used synthetic spectra (with known atmospheric parameters and  $[\text{C}/\text{Fe}]$ ) from our grid covering three fixed metallicities,  $[\text{Fe}/\text{H}] = -1.0, -1.5$ , and  $-2.5$ , three fixed gravities,  $\log g = 2.0, 3.0$ , and  $4.0$ , which spans the range of the majority of our program stars, and two levels of carbonicity,  $[\text{C}/\text{Fe}] = 0.0$  and  $[\text{C}/\text{Fe}] = +1.5$ . We then intentionally perturbed their input  $\log g$  values by  $-1.0$  dex,  $-0.5$  dex,  $+0.5$  dex, and  $+1.0$  dex, and derived estimates of their  $[\text{C}/\text{Fe}]$  following the procedures described above. As can be seen from inspection of Figure 3 (which shows the case for  $[\text{C}/\text{Fe}] = 0.0$ ), the effects on estimates of  $[\text{C}/\text{Fe}]$  never exceed 0.5 dex (and then only in the most extreme cases of  $\pm 1.0$  dex variation in  $\log g$ ), and are generally much smaller than that. Not surprisingly, the largest variations occur for the warmest stars, which have weaker CH G-band features. However, our sample included only a small fraction of stars with  $T_{\text{eff}} > 6500 \text{ K}$  ( $\sim 3\%$ ), so this is not expected to have a major effect. The mean zero-point offsets and rms variations in the derived  $[\text{C}/\text{Fe}]$ , relative to the known value across all  $T_{\text{eff}}$  and  $\log g$  considered, are shown for each panel in Figure 3, and are acceptably small. Similar results apply to the case when we fix the input  $[\text{C}/\text{Fe}] = +1.5$ . Figure 3 considered the solar  $[\text{C}/\text{Fe}]$  case, since we are more concerned with false positives that would cause us to count a star as carbon-enhanced when it is not. We conclude that, while some sensitivity to estimates of  $[\text{C}/\text{Fe}]$  may exist due to errors in estimates of  $\log g$ , its impact on our results should be minimal, except for truly extreme cases.

#### 2.4. Detections, Upper Limits, and First-Pass Frequencies of CEMP Stars

In this work there are 31187 unique stars for which estimates of  $[\text{C}/\text{Fe}]$  were carried out (other objects were either repeats, in which case they were averaged, had insufficient spectral S/N ratios, were clear cases of QSOs, cool white dwarfs, or very late-type stars, or had some spectral defect in the region of the CH G-band which prevented measurements being obtained – all such stars are dropped from the subsequent analysis). The remaining sample can be divided into two categories: stars that have a measured  $[\text{C}/\text{Fe}]$  (with the G-band detected;  $N^D = 25647$ ), and stars for which only an upper limit on  $[\text{C}/\text{Fe}]$  has been obtained (G-band undetected;  $N^L = 5540$ ). We call the associated two sets of stars subsample D and subsample L, respectively. Figure 4 shows  $[\text{C}/\text{Fe}]$  as a function of metallicity for these two categories. The “ridge lines” in both of the panels are due to grid effects in the chi-square matching procedure. It is worth noting that most of the stars with mea-

sured  $[\text{C}/\text{Fe}]$  (subsample D) exhibit carbonicity below  $[\text{C}/\text{Fe}] = +0.7$ , which indeed appears to be a natural dividing threshold between carbon-normal stars and carbon-rich stars. This limit was also established by Aoki et al. (2007b), who also included in their analysis expected evolutionary effects on the definition of CEMP stars. We adopt this value of  $[\text{C}/\text{Fe}]$  to define the carbon-rich stars in our sample, without making any luminosity correction adjustment, since our sample includes very few cool giants. There is an evident correlation between  $[\text{C}/\text{Fe}]$  and  $[\text{Fe}/\text{H}]$  seen in this figure, in particular for stars with  $[\text{Fe}/\text{H}] < -1.0$ . The relative number of stars with carbon excesses increases as the metallicity decreases, as does the level of carbonicity, as reported previously by several studies based on much smaller samples of stars.

Adopting the definition of carbon-rich stars as above, we distinguish two subcategories within subsamples D and L: stars with  $[\text{C}/\text{Fe}] \leq +0.7$  (C-norm), and stars with  $[\text{C}/\text{Fe}] > +0.7$  (C-rich). In the case of subsample L, the carbon status for a star can be assessed with certainty only when  $[\text{C}/\text{Fe}] \leq +0.7$ , and remains unknown for stars having  $[\text{C}/\text{Fe}] > +0.7$ . Indeed, suppose that the limit assigned to a given star is  $[\text{C}/\text{Fe}]_{\text{lim}} = +1.5$ . Then, all values below  $[\text{C}/\text{Fe}]_{\text{lim}}$  can still be accepted for that star, including carbonicity well below  $[\text{C}/\text{Fe}] = +0.7$ . When the upper limit is below  $[\text{C}/\text{Fe}] = +0.7$ , however, the carbon status of the star can be assessed as C-norm. Not surprisingly, there is a strong temperature effect in the assessment of the carbon status for stars in our sample. For example, stars with higher  $T_{\text{eff}}$  (above  $T_{\text{eff}} \sim 6250$  K) would require quite high  $[\text{C}/\text{Fe}]$  for the CH G-band to be detected; stars without a detected CH G-band are included in the L subsample. Thus, the fractions of CEMP stars we derive in this paper are lower limits to the true fractions. In a future paper we plan to obtain an explicit correction function to account for the “missing” stars due to this temperature effect, in order to assess its impact on the derived frequencies of CEMP stars.

Taking into account the above definitions, the fraction of C-rich stars can be formulated as:

$$F_{\text{C-rich}} = \frac{N_{\text{C-rich}}^{\text{D}}}{N_{\text{C-rich}}^{\text{D}} + N_{\text{C-norm}}^{\text{D}} + N_{\text{C-norm}}^{\text{L}}} \quad (2)$$

where  $N_{\text{C-norm}}^{\text{D}}$  and  $N_{\text{C-rich}}^{\text{D}}$  are stars belonging to subsample D and having  $[\text{C}/\text{Fe}] \leq +0.7$  and  $[\text{C}/\text{Fe}] > +0.7$ , respectively, while  $N_{\text{C-norm}}^{\text{L}}$  are stars in subsample L and having  $[\text{C}/\text{Fe}] \leq +0.7$ . Stars with unknown carbon status are not included in the above definition.

Table 2 reports the number of stars belonging to the various categories for different ranges of metallicity, as well as the total fractions of C-rich stars. Note that, when comparing the reported fractions in this table with other fractions reported in this paper, the Table 2 fractions have no restriction on whether or not acceptable proper motion and radial velocity measurements were available for a given star.

### 3. THE NATURE OF THE CARBON-RICH STAR SAMPLE

#### 3.1. Radial Velocities, Distance Estimates, and Definition of the Extended and Local Samples

We begin with the 31187 unique DR7 calibration stars for which estimates of  $[\text{C}/\text{Fe}]$  exist, and with distances slightly revised from those presented in C07 and C10, as described below. Details concerning the nature of the calibration-star

sample can be found in C10; here we recall a few facts concerning these stars that are of importance for the present analysis.

Spectra of the SDSS/SEGUE calibration stars were obtained to perform spectrophotometric corrections and to calibrate and remove the night-sky emission and absorption features (telluric absorption) from SDSS spectra. The spectrophotometric calibration stars cover the apparent magnitude range  $15.5 < g_0 < 17.0$ , and satisfy the color ranges  $0.6 < (u-g)_0 < 1.2$ ;  $0.0 < (g-r)_0 < 0.6$ .<sup>3</sup> The telluric calibration stars cover the same color ranges as the spectrophotometric calibration stars, but at fainter apparent magnitudes, in the range  $17.0 < g_0 < 18.5$ .

The C10 paper describes the radial velocity estimates (which have a precision of 5-20 km s<sup>-1</sup>, depending on the S/N ratio of the spectrum, and with a negligible zero-point offset), as well as photometric distance estimates, obtained by using the SSPP surface-gravity estimate for luminosity classification, then following the procedures of Beers et al. (2000). Since the estimated  $\log g$  is used only for classification, this means that for stars redder than than main-sequence turnoff (MSTO), the expected large differences in surface gravity for dwarfs and giants make even approximate  $\log g$  estimates sufficient – errors of 1 to 2 dex in  $\log g$  would have to be routinely made in order to confound this procedure. Close to the MSTO, any method of photometric distance estimation becomes more problematic, but the difference in the derived distances for stars just above or just below the MSTO decreases the closer they are to it, which mitigates against these effects.

Schönrich et al. (2011) have criticized the Beers et al. (2000) method of distance determination, and the results of the C07 and C10 that relied on it. They claimed that the counter-rotating halo found in C07 and C10 is a result of biases in distance estimates for main-sequence dwarfs, and furthermore that the distance derivation is influenced by sorting a subset of the stars into incorrect positions in the color-magnitude diagram of an old, metal-poor population. In a rebuttal paper, Beers et al. (2011) demonstrated that the Schönrich et al. claims concerning dwarf distances are incorrect (due to their adoption of the wrong main-sequence absolute magnitude relationship from Ivezić et al. 2008). Furthermore, the claimed retrograde tail in the rotation-velocity distribution was shown to arise from the measured asymmetric proper motions, and was not the result of the propagation of distance errors. In any event, we have applied the procedure suggested in the rebuttal paper to reassign intermediate-gravity stars that were originally classified as main-sequence turnoff stars into dwarf or subgiant/giant luminosity classifications, in cases where their derived  $T_{\text{eff}}$  were substantially lower than expected for the turnoff. Revised distances for these stars have been adopted as well. A reassessment of the kinematics indicates that the retrograde signal for the subsample at very low metallicity ( $[\text{Fe}/\text{H}] < -2.0$ ) remains. The interested reader can find more details in Beers et al. (2011). Based on the discussion in that paper, we believe that our distances should be accurate to on the order of 15-20%.

The C10 procedures applied a series of cuts to their sample designed to better enable measurement of the kinematic and orbital properties of the various stellar populations considered. This produced a subsample of stars in the local vol-

<sup>3</sup> The subscript 0 in the magnitudes and colors indicates that they are corrected for the effects of interstellar absorption and reddening, based on the dust maps of Schlegel et al. (1998).

ume (distance from the Sun  $d < 4$  kpc, and with  $7 \text{ kpc} < R < 10$  kpc, where  $R$  is the Galactocentric distance projected onto the plane of the Galaxy), which they referred to as the “Local Sample” ( $N \sim 17000$ ). These restrictions were made in order to mitigate against the increase in the errors in the derived transverse velocities, which scale with distance from the Sun, and to improve the applicability of the simple models for the adopted form of the Galactic potential. For our present analysis we do not need to redetermine the velocity parameters of the underlying stellar populations, so we can relax these cuts somewhat. As described below, in order to increase the numbers of stars in our sample with measured  $[C/Fe]$ , we have changed the constraint on the distance from the Sun, from  $d < 4$  kpc to  $d < 10$  kpc, and removed the constraint on the projected distance  $R$ . With these relaxed cuts the total number of stars climbs to 30874. We refer to this new sample as the “Extended Sample.”

The upper panel of Figure 5 shows the as-observed metallicity distribution function (MDF) for the DR7 calibration stars belonging to the Extended Sample (black histogram), as well as for stars in the C10 Local Sample, as described above (red histogram). We use the term “as-observed” in order to call attention to the fact that the selection functions for the calibration stars were not intended to return a fair sample of stars, suitable for an unbiased analysis of the distribution of metallicity for stars in the Galaxy. Rather, the calibration stars were selected to emphasize the numbers of moderately low-metallicity stars that might serve to best constrain the spectrophotometry and telluric line corrections carried out as part of the SDSS spectroscopic pipeline reductions. Thus, these MDFs are a “sample of convenience,” one that is still useful for providing guidance as to the presence of various stellar populations in metallicity space, but not for obtaining estimates of their relative normalizations (for which other samples drawn from SDSS are more suitable). No selection for or against carbon-enhanced stars was carried out in the selection of the calibration-star sample.

The MDFs of the two samples are clearly very similar, and comprise stars with metallicities that sample all of the primary stellar components of the Galaxy (with the exception of the bulge). The lower panel of Figure 5 is the distribution of  $[C/Fe]$  (estimated as described above), which we refer to as the carbonicity distribution function (CarDF) for the Extended Sample (black histogram), and for the Local Sample (red histogram)<sup>4</sup>. The inset in the panel shows a rescaling appropriate for the high  $[C/Fe]$  tail of this distribution. As in the case of the MDFs, the shape of the two CarDFs are similar, with a strong peak at  $[C/Fe] \sim +0.2$  to  $+0.3$ , and two tails, a weak one at low carbonicity ( $[C/Fe] < 0$ ), and a strong one that extends to high carbonicity,  $+0.5 < [C/Fe] < +3.0$ . The total number of stars with high carbonicity is significantly different in the two samples. Indeed, for the Extended Sample we find 728 stars with  $[C/Fe] > +0.7$ , while for the Local Sample the number is reduced to 318.

### 3.2. As-Observed MDF and CarDF of the Extended Sample as a Function of Distance from the Galactic Plane

We now examine the MDFs and the CarDFs of the Extended Sample of calibration stars for different intervals in  $|Z|$ , with cuts chosen to ensure there remain adequate num-

bers of stars in each interval.

In Figure 6, the first (left-hand) column and the third column show the MDFs, while the second column and the fourth (right-hand) column are the CarDFs. In the first and third columns, the red arrows indicate the peak metallicities of the various stellar populations considered by C10. In the second and fourth column, the blue arrows show the location of the solar carbon-to-iron ratio ( $[C/Fe] = 0.0$ ), and the location of the natural threshold that divides carbon-normal stars from carbon-rich stars ( $[C/Fe] = +0.7$ ), as identified above.

Examination of the first column of panels in Figure 6 shows how the MDF changes from the upper-left panel, in which there are obvious contributions from the thick-disk, the metal-weak thick disk (MWTD), and inner-halo components in the cuts close to the Galactic plane, to the lower-left panel, with an MDF dominated primarily by inner-halo stars. In the third column of panels, with distances from the plane greater than 5 kpc, the transition from inner-halo dominance to a much greater contribution from outer-halo stars is clear. This demonstration is, by design, independent of any errors that might arise from derivation of the kinematic parameters, and provides confirmation of the difference in the chemical properties of the inner- and outer-halo populations originally suggested by C07. The second and fourth columns show the results of the same exercise for the CarDFs. Close to the Galactic plane (second column; up to  $|Z| = 3$  kpc), where the thick disk and MWTD are the dominant components, the CarDF is strongly peaked at values between  $[C/Fe] = 0.0$  and  $[C/Fe] = +0.3$ . The CarDFs of the thick disk and MWTD will be explored in a future paper. Here we simply note that in the regions close to the plane, where these components dominate the sample, there are not many stars populating regions of high carbonicity. At larger distances from the Galactic plane, where the inner halo begins to be the dominant component, there appears a tail in the carbonicity distribution towards higher values,  $[C/Fe] > +0.5$ . In the fourth column of panels, where the distance from the Galactic plane is  $|Z| > 5$  kpc, and where we expect to see the beginning of the transition from inner-halo dominance to outer-halo dominance, the tails towards high  $[C/Fe]$  values become even more evident. The CarDF exhibits a strong peak at  $[C/Fe] \sim +0.3$  and a long tail towards high values of carbonicity, up to  $[C/Fe] = +3.0$ . The nature of the CarDF is likely to be influenced by the change of the MDF as a function of the distance from the Galactic plane, due the well-known trend of increasing  $[C/Fe]$  with declining  $[Fe/H]$ . However, as discussed below, there is evidence that the observed changes may reflect *real differences* in the chemistry of the inner- and outer-halo populations, even at a given (low) metallicity.

By adopting the threshold of  $[C/Fe] > +0.7$ , the fraction of SDSS/SEGUE calibration stars with high carbonicity in the subsample at  $|Z| > 9$  is 20%, (which, as argued above, is a lower limit), in line with previous estimates for stars with  $[Fe/H] < -2.0$ .

### 3.3. Comparisons of Distance and Rotational Velocity Distributions for CEMP and non-CEMP Stars

We now consider how the nature of our Extended Sample differs for the low-metallicity ( $[Fe/H] < -1.5$ ) CEMP ( $[C/Fe] > +0.7$ ) and non-CEMP ( $[C/Fe] < +0.7$ ) stars. Figure 7 shows two columns of panels, corresponding to the stars in our sample with different cuts on  $Z_{max}$  (the maximum distance of a stellar orbit above or below the Galactic plane); the left-

<sup>4</sup> We employ the term “carbonicity distribution function” to emphasize that we are describing the carbon-to-iron abundance ratio, rather than the carbon abundance distribution itself.



hand column includes stars at all  $Z_{\max}$ , while the right-hand column only include stars satisfying  $Z_{\max} > 5$  kpc. The top panels show the distributions of distance,  $d$ , while the bottom panels are the distribution of the Galactocentric rotational velocity,  $V_\phi$ . For all panels, CEMP stars are shown as red dot-dashed histograms; non-CEMP stars are shown as black solid histograms.

As can be seen in the top panel of each column, the peak of the distance distribution in both cases is, for the non-CEMP stars,  $d \sim 2$  kpc, while for the CEMP stars, a softer peak is seen around  $d \sim 2.5$ –4 kpc (closer to  $d \sim 4$  kpc for the higher  $Z_{\max}$  cut), with long tails extending to the 10 kpc cutoff of the Extended Sample. At all distances beyond  $d \sim 3$  kpc the relative fraction of CEMP stars exceeds that of the non-CEMP stars, while closer than  $d \sim 3$  kpc the relative fraction of non-CEMP stars is greater than that of the CEMP stars. A Kolmogorov-Smirnov (K-S) test of the distance distributions indicates that the hypothesis that the CEMP and non-CEMP stars are drawn from the same parent population is rejected at high significance ( $p < 0.001$ ) for both cuts on  $Z_{\max}$ .

For the case of  $Z_{\max} > 0$  kpc, stars classified as dwarfs represent 72% of the non-CEMP sample and 42% of the CEMP sample, while subgiants and giants represent 24% of the non-CEMP sample and 50% of the CEMP sample. For both the non-CEMP and CEMP samples, main-sequence turnoff stars represent less than 10% of the samples. For the case of  $Z_{\max} > 5$  kpc, dwarfs comprise 52% of the non-CEMP sample and 29% of the CEMP sample, while subgiants/giants represent 44% of the non-CEMP sample and 63% of the CEMP sample. Again, main-sequence turnoff stars comprise less the 10% of both samples. Thus, the difference in distance distribution is not solely dependent on the luminosity classes associated with the populations split on carbonicity; dwarfs and subgiants/giants are both significantly represented in each of the non-CEMP and CEMP samples.

From inspection of the bottom panels of Figure 7, the non-CEMP stars exhibit a slightly asymmetric distribution of rotational velocities centered close to  $V_\phi \sim 0$  km s $^{-1}$ , and a weak retrograde tail. By contrast, the CEMP stars exhibit a rather strong asymmetry extending to large retrograde velocities. A K-S test of the rotational-velocity distributions indicates that the hypothesis that the CEMP and non-CEMP stars are drawn from the same parent population is rejected at high significance ( $p < 0.001$ ) for both cuts on  $Z_{\max}$ .

It is interesting to consider the distribution of luminosity classes for the split on  $[C/Fe]$  for the retrograde stars with  $V_\phi < -100$  km s $^{-1}$ . For the case of  $Z_{\max} > 0$  kpc, stars in the retrograde tail classified as dwarfs represent 66% of the non-CEMP sample and 20% of the CEMP sample, while subgiants/giants represent 30% of the non-CEMP sample and 73% of the CEMP sample. For both non-CEMP and CEMP samples main-sequence turnoff stars represent less than 10% of the samples. For the case of  $Z_{\max} > 5$  kpc, the retrograde stars classified as dwarfs comprise 48% of the non-CEMP sample and 18% of the CEMP sample, while subgiants/giants represent 47% of the non-CEMP sample and 75% of the CEMP sample. Again, main-sequence turnoff stars comprise less than 10% of both samples. Significant fractions of dwarfs and giants are present in the retrograde tail for both the non-CEMP and CEMP samples. Thus, the retrograde signature is unlikely to be due to a preponderance of stars with aberrant distance estimates owing to luminosity misclassifications.

If we specialize to the highly retrograde tails, we find that

for  $Z_{\max} > 0$  kpc, the portion of the non-CEMP sample in this tail is only 8% for  $V_\phi < -150$  km s $^{-1}$  and 4% for  $V_\phi < -200$  km s $^{-1}$ . For the CEMP stars, these portions are 17% for  $V_\phi < -150$  km s $^{-1}$  and 12% for  $V_\phi < -200$  km s $^{-1}$ , respectively. For the case of  $Z_{\max} > 5$  kpc, the portion of the non-CEMP sample is 12% for  $V_\phi < -150$  km s $^{-1}$  and 8% for  $V_\phi < -200$  km s $^{-1}$ . For the CEMP stars, these portions are 24% for  $V_\phi < -150$  km s $^{-1}$  and 19% for  $V_\phi < -200$  km s $^{-1}$ , respectively. Thus, in both cases, a split on the level of carbon enhancement leads directly to rather different relative population of the retrograde tails, compared to the full distributions of non-CEMP and CEMP stars. Identifying the highly retrograde tails with the outer-halo population, we can already infer that the outer-halo component appears to harbor a greater fraction of CEMP stars than the inner-halo component.

In addition, before considering a more complete discussion below, we can make use of the  $V_\phi$  distribution to obtain an estimate of the approximate fraction of CEMP stars in the outer halo. We proceed by asserting that the stars in the highly retrograde tail, with  $V_\phi < -200$  km s $^{-1}$ , are very likely to be members of the outer-halo population. This follows because the dispersion in  $V_\phi$  for an essentially non-rotating inner halo is on the order of 100 km s $^{-1}$ , and placing a cut at two sigma below the mean rotation of the inner halo excludes all but 2.5% of likely inner-halo stars. With this assumption, we find that 11% of the stars in the highly retrograde tail (and with  $Z_{\max} > 5$ ) kpc are CEMP stars. This differs from the calculations immediately above, in that we are considering the fractions of CEMP stars relative to the total number of stars (including those from the L subsample, but not those with unknown carbon status; i.e., we are using Eqn. 2). Recall that this calculation applies only for stars with  $[Fe/H] < -1.5$ . For this subsample we find a mean carbonicity of  $\langle [C/Fe] \rangle = +1.47 \pm 0.07$ , where the error is the standard error of the mean. This value can be taken as a first-pass estimate of the mean outer-halo carbonicity.

Figure 8 shows the observed distributions of the measured proper motions in the right ascension and declination directions for the low-metallicity ( $[Fe/H] < -1.5$ ) stars in our sample, for two cuts on  $Z_{\max}$ , represented by small blue dots. The same panels show, represented as red stars, the objects that populate the highly retrograde tails of the distribution of rotational velocity shown in Figure 7. Note that cuts at  $V_\phi < -150$  km s $^{-1}$  and  $V_\phi < -200$  km s $^{-1}$  are shown in the upper and lower rows of panels, respectively. As can be appreciated from inspection of this figure, the proper motions in both directions for the stars assigned to the highly retrograde tail are asymmetrically distributed, and explore much larger values, relative to the rest of the sample. This supports the reality of the highly retrograde signature seen in Figure 7, and indicates that it is due primarily to the proper motions of the participating stars. See Beers et al. (2011) for additional details concerning the veracity and interpretation of SDSS proper motions for the SDSS calibration-star sample.

#### 4. EXTREME DECONVOLUTION AND MEMBERSHIP PROBABILITIES

In the relatively nearby volume explored by the SDSS/SEGUE calibration-star sample, C07 and C10 have shown that the two stellar components of the Galactic halo are strongly overlapped in their spatial distribution, velocity ellipsoids, and MDFs. Thus, to explore possible

differences in the frequencies and mean carbonicities of CEMP stars, it is essential to assign inner- and outer-halo membership probabilities to each star in the sample that is likely to belong to the halo system. We describe how this is accomplished in the sections below.

#### 4.1. Basic Parameters

In the solar neighborhood, the set of parameters that best identify the presence of the main structures are the distance from the Galactic plane, the rotational velocity of a star in a cylindrical frame with respect to the Galactic center, and the stellar metallicity (see C10). For consideration of the disk system of the Galaxy, the distance from the Galactic plane is best represented by  $|Z|$  (the present distance of a star above or below the Galactic plane), while for the halo components, a more suitable distance is  $Z_{\max}$ , which depends on the adopted gravitational potential. The choice of  $Z_{\max}$  for the Galactic halo is necessary because of the much larger spatial extent of its two primary components, relative to that of the disk components.

Before seeking a deconvolution of the inner- and outer-halo components, we need to check for possible correlations between all of the basic parameters we wish to employ. In C10 we have shown that  $Z_{\max}$  has a significant correlation with  $V_R$  and  $V_Z$ , but not with  $V_\phi$ , other than that expected from the presence of the thick-disk population at high positive rotation velocity and the halo at lower rotational velocity. A very similar behavior is confirmed for the Extended Sample as well (Figure 9). We conclude that the Galactocentric rotational velocity,  $V_\phi$ , and the vertical distance,  $Z_{\max}$ , when combined with metallicity, can be used to obtain useful information on the different stellar populations present in the Extended Sample.

The primary chemical parameter of the present analysis is the carbonicity,  $[C/Fe]$ , so it is important to check for its possible correlations with the basic parameters defined above. The result of this exercise is shown in Figure 10. Here, the upper panel shows the Galactocentric rotational velocity as a function of metallicity for the Extended Sample. The gray dots represent the stars in the sample with  $[C/Fe] < +0.7$ , while the red dots denote the stars with enhanced carbonicity,  $[C/Fe] > +0.7$ . It is worth noting that the stars with  $[C/Fe] > +0.7$  are *almost all* located in the halo components of the Galaxy, with few exceptions. This is perhaps not surprising, as the halo components of the Milky Way are very metal poor. The middle panel of Figure 10 shows the Galactocentric rotational velocity,  $V_\phi$ , as a function of  $[C/Fe]$ . This plot shows no evidence of correlation between  $V_\phi$  and  $[C/Fe]$ . Finally, the lower panel of Figure 10 shows  $[Fe/H]$  as a function of  $[C/Fe]$ . Here, there is clear evidence of a correlation between  $[C/Fe]$  and  $[Fe/H]$  – the carbonicity increases as the metallicity decreases. A similar trend was already noticed in past works, such as Rossi et al. (2005) and Lucatello et al. (2006). We consider this result in more detail below.

#### 4.2. CEMP Fractions in the Low Metallicity Regime: Global Behavior

The left panel of Figure 11 shows the fraction of CEMP stars in the Extended Sample, as a function of  $[Fe/H]$ , in the metal-poor regime ( $[Fe/H] < -1.5$ ), and at vertical distance  $Z_{\max} > 5$  kpc (chosen to avoid thick disk and MWTD contamination). Here, each bin in metallicity corresponds to an interval of  $\Delta[Fe/H] = 0.2$  dex, with the exception of the last

bin, where stars are selected in the range  $[Fe/H] < -2.6$ . The fractions of CEMP stars in each bin are obtained by selecting objects with  $[C/Fe] > +0.7$ , and application of Eqn. 2. Errors on the CEMP fraction are evaluated through the jackknife approach. This technique is similar to bootstrapping, but instead of sampling with replacement, it recomputes the statistical estimate leaving out one observation at a time from the sample (Wall & Jenkins 2003). The dash-dotted line is a second-order polynomial fit to the data.

The increase of the fraction of CEMP stars with declining metallicity pertains to the global behavior of the data in the metal-poor regime. If metallicity alone is the driver of the carbon-enhancement phenomenon, one might wonder if the strong increase in the fraction of CEMP stars at  $[Fe/H] < -2.0$  could be due to the increasing importance of the outer-halo component, which has a peak of metallicity at  $[Fe/H] \sim -2.2$ , and a long tail extending to lower metallicity.

We have evaluated the as-observed fractions of carbon-rich stars in our Extended Sample, for  $Z_{\max} > 5$  kpc, over several bins in metallicity. With the adopted definition of carbon-rich stars ( $[C/Fe] > +0.7$ ), and following Eqn. 2, we find that 2%, 7%, and 20% of stars in the intervals  $-1.5 < [Fe/H] < -0.5$ ,  $-2.5 < [Fe/H] < -1.5$ , and  $[Fe/H] < -2.5$ , are carbon-rich, respectively. For ease of comparison with previous determinations of the CEMP fractions in the halo, we note that the global fraction of CEMP stars in the halo system with  $Z_{\max} > 5$  kpc and  $[Fe/H] < -1.5$  is 8%, for  $[Fe/H] < -2.0$  it is 12%, and for  $[Fe/H] < -2.5$  it is 20%.

The right panel of Figure 11 shows the mean carbonicity,  $\langle[C/Fe]\rangle$ , as a function of  $[Fe/H]$ . Obviously, it is a strong function of metallicity, although there may be some sign of it leveling off at the lowest metallicities. Larger samples, in particular of lower metallicity CEMP stars, are required to be certain.

Figure 12 shows the fraction of CEMP stars in the Extended Sample, as a function of distance from the Galactic plane,  $|Z|$ , for stars satisfying  $-2.0 < [Fe/H] < -1.5$  and  $[Fe/H] < -2.0$ , respectively. The intervals for the cuts on height above or below the plane have widths of  $\Delta|Z| = 4$  kpc, and the CEMP star fractions in each bin are obtained by applying the same criteria and definitions as used for the left panel of Figure 11. In the range of metallicity  $-2.0 < [Fe/H] < -1.5$ , significant contamination of the sample from thick-disk stars is not expected, while the MWTD could be still present (with metallicity peak around  $[Fe/H] \sim -1.3$ ), but only in the region close to the Galactic plane ( $0 \text{ kpc} < |Z| < 4 \text{ kpc}$ ); the MWTD would not be expected to contribute for the metallicity range  $[Fe/H] < -2.0$  even close to the plane. Inspection of this figure indicates a clear dependence of the CEMP star fraction on distance from the Galactic plane. Close to the plane, this dependence is due to the combined presence of the possible MWTD and inner-halo populations, while at  $|Z| > 4$  kpc, the observed fractions must essentially pertain to the halo system alone. Far from the Galactic plane, the observed increase of the CEMP star fractions with  $|Z|$  would be difficult to understand if the halo system comprises a single population. In such a case, one might expect the CEMP star fractions to be roughly constant, as a function of  $|Z|$ , for any given cut in metallicity. This is clearly *not* what the data show.

Interestingly, we note that, for the same intervals in  $|Z|$ , the mean carbonicity remains approximately constant, at a value  $\langle[C/Fe]\rangle \sim +1.0$  for  $-2.0 < [Fe/H] < -1.5$  and  $\langle[C/Fe]\rangle \sim +1.5$  for  $[Fe/H] < -2.0$ . Of course, the contribution from the inner- and outer-halo components is shifting as one pro-

gresses from low to high  $|Z|$ , and this may be smoothing out any real variations associated with the individual components. We return to this question below.

A similar trend of increasing CEMP star fraction with height above the Galactic plane was previously suggested by Frebel et al. (2006), based on a much smaller sample of stars from the Hamburg/ESO survey (Wisotzki et al. 2000; Christlieb 2003), and proportionately larger error bars. Our expanded data set now clearly indicates the existence of a strong spatial variation of the CEMP star frequency *within the halo system*, and suggests that the observed carbon enhancement is unlikely to be purely driven by metallicity alone. Rather, it points to a real difference in CEMP star fractions associated with the inner- and outer-halo populations, and opens the possibility for different carbon-production mechanisms and/or different chemical-evolution histories within their progenitors. We return to this question below, after considering a method to probabilistically classify individual stars as likely inner- or outer-halo members.

#### 4.3. The Extreme Deconvolution Technique

Inference of the distribution function of an observable given only a finite, noisy set of measurements of that distribution is a problem of significant interest in many areas of science, and in astronomy in particular. The observed distribution of a parameter is just the starting point, but what is desired is knowledge of the distribution that we would have in the case of very small uncertainties of the data and with all of the dimensions of the parameter measured; in other words, the closest representation of the underlying distribution. Usually, the data never have these two properties, and it is then challenging to find the underlying distribution without taking into account the uncertainty of the data (Bovy, Hogg, & Roweis, 2011; hereafter BHR11). The Extreme Deconvolution (XD) technique of BHR11 confronts all of these issues, and provides an accurate description of the underlying distribution of a  $d$ -dimensional quantity by taking into account the potentially large and heterogeneous observational uncertainties, as well as missing dimensions.

The BHR11 paper generalized the well known mixtures-of-Gaussians density-estimation method to the case of noisy, heterogeneous, and incomplete data. In this method, the underlying distribution of a quantity  $\mathbf{v}$  is modeled as a sum of  $K$  Gaussian distributions

$$p(\mathbf{v}) = \sum_{j=1}^K \alpha_j N(\mathbf{v}|\mathbf{m}_j, \mathbf{V}_j), \quad (3)$$

where the function  $N(\mathbf{v}|\mathbf{m}_j, \mathbf{V}_j)$  is the  $d$ -dimensional Gaussian distribution with mean  $\mathbf{m}$  and variance tensor  $\mathbf{V}$  and  $\alpha_j$  are the amplitudes, normalized to sum to unity (all of these parameters are grouped together as  $\theta$  in what follows). The data  $\mathbf{w}_i$  are assumed to be noisy samples from this distribution

$$\mathbf{w}_i = \mathbf{v}_i + \text{noise}, \quad (4)$$

where the noise is drawn from a normal distribution with zero mean and known covariance matrix  $\mathbf{S}_i$ . Here and in what follows, we ignore the projection matrices  $\mathbf{R}_i$  of BHR11, since the data we will apply this technique to are complete.

The likelihood of the model for each data point is given by the model convolved with the uncertainty distribution of that data point. Since a Gaussian distribution convolved with another Gaussian distribution is again a Gaussian, the likelihood

for each data point is a sum of Gaussian distributions

$$p(\mathbf{w}_i|\theta) = \sum_{j=1}^K \alpha_j N(\mathbf{w}_i|\mathbf{m}_j, \mathbf{T}_{ij}) \quad (5)$$

where

$$\mathbf{T}_{ij} = \mathbf{V}_j + \mathbf{S}_i. \quad (6)$$

The objective function is the total likelihood, obtained by simply multiplying the individual likelihoods together for the various data points

$$\ln \mathcal{L} = \sum_i \ln p(\mathbf{w}_i|\theta) = \sum_i \ln \sum_{j=1}^K \alpha_j N(\mathbf{w}_i|\mathbf{m}_j, \mathbf{T}_{ij}). \quad (7)$$

The optimization of this objective function provides the maximum likelihood estimate of the distribution, or its parameters. In BHR11, the authors developed a fast and robust algorithm to optimize the likelihood, based on an adaptation of the expectation-maximization algorithm<sup>5</sup> (Dempster et al. 1977).

The XD technique provides the best-fit values of the amplitude, mean, and standard deviation of each Gaussian component, as well as the so-called *posterior probability* that the observed data point  $\mathbf{w}_i$  is drawn from the component  $j$ . The posterior probability is given by

$$p_{ij} = \frac{\alpha_j N(\mathbf{w}_i|\mathbf{m}_j, \mathbf{T}_{ij})}{\sum_k \alpha_k N(\mathbf{w}_i|\mathbf{m}_k, \mathbf{T}_{ik})}, \quad (8)$$

(see BHR11 for the derivation of this formula). The posterior probability is a powerful statistical tool to perform probabilistic assignments of stars to a Gaussian component in the model distribution. In Galactic studies, the Gaussian component could represent a primary structural component such as a disk or halo, a moving group, or a spatial or velocity overdensity.

In many respects the XD technique described above is similar to the maximum likelihood technique adopted in C10, but is more general, because it takes into account the uncertainties of the measurements and provides the membership probabilities.

#### 4.4. Application to the SDSS/SEGUE DR7 Calibration Stars

The basic parameters for application of the XD approach for the analysis at hand are the Galactocentric rotational velocity,  $V_\phi$ , the maximum vertical distance,  $Z_{\max}$ , and the metallicity,  $[\text{Fe}/\text{H}]$ . We employ the XD technique to determine the underlying distribution of the rotational velocity of halo stars and to determine the posterior membership probabilities for each star. In practice, the entries for the XD algorithm are the Galactocentric rotational velocity and its uncertainty for each star,  $V_{\phi,i}$  and  $\varepsilon_{V_{\phi,i}}$ , respectively<sup>6</sup>. These two parameters, together with all of the other kinematic and orbital quantities, are derived using the same procedures employed by C07 and C10 (but with revised distances for the reassigned main-sequence turnoff stars, as discussed above).

<sup>5</sup> Code implementing this algorithm is available at <http://code.google.com/p/extreme-deconvolution/>.

<sup>6</sup> Note that errors in the rotational velocity depend in turn on errors in the distances and proper motions; these are carried forward into the analysis automatically.



Our plan is to make use of a sample in which the constraint on the distance from the Sun,  $d$ , and on the projected Galactic distance,  $R$ , are relaxed (in order to take advantage of the larger numbers of CEMP stars in the Extended Sample). As a consequence, the data set becomes noisier than the Local Sample, because uncertainties on the transverse velocities increase with the distance  $d$ . In the terminology of the XD approach, the analysis of the Extended Sample falls into the case where all the observables are known, but some of the derived parameters have large uncertainties.

The Galactic halo is assumed to be a two-component structure, comprising the inner and the outer halo, as discussed in C07 and C10. Thus, the general expression for the likelihood takes the form:

$$\ln \mathcal{L} = \sum_i \ln[\alpha_{in} \cdot N_{in}^i + \alpha_{out} \cdot N_{out}^i], \quad (9)$$

where  $\alpha_{in}$  and  $\alpha_{out}$  are the amplitude of the inner halo and outer halo, respectively. The velocity distributions are assumed to be Gaussian, thus

$$N_{in/out}^i = N(V_{\phi,i} | V_{\phi,in/out}, \sigma_{\phi,in/out}^2 + \varepsilon_{V_{\phi},i}^2), \quad (10)$$

The membership probabilities then take the form:

$$p_{i,in} = \frac{\alpha_{in} N_{in}^i}{\alpha_{in} N_{in}^i + \alpha_{out} N_{out}^i} \quad (11)$$

and

$$p_{i,out} = \frac{\alpha_{out} N_{out}^i}{\alpha_{in} N_{in}^i + \alpha_{out} N_{out}^i} \quad (12)$$

for the  $i$ th star.

#### 4.4.1. Extreme Deconvolution Results for the Extended Sample

In this section the posterior probabilities, derived through the application of the XD, are obtained for the Extended Sample ( $d < 10$  kpc, no constraints on  $R$ ), selected in the range of metallicity  $[\text{Fe}/\text{H}] < -2.0$ , and with vertical distance  $Z_{\text{max}} > 5$  kpc. The results are shown in Figure 13. The upper panel of this figure shows the distribution of the observed rotation velocity  $V_{\phi}$  (black histogram), and the green and red curves represent the resulting Gaussian velocity distributions for the inner- and outer-halo components. The middle panel shows the derived velocity distribution for the two components, obtained by weighting each star with its membership probability, and normalized such that the total area corresponds to unity. The black histogram is the observed distribution as in the top panel, but normalized to unity as well. In the lower panel, the posterior probability as a function of the rotational velocity,  $V_{\phi}$ , is shown. This probability has been obtained using Eqns. 11 and 12. For each star in the sample, the XD technique assigns two probability values, the first associated with the inner halo, and the second related to the outer halo. Since in our model a star is required to belong to one or the other component (there are no orphans allowed), and the summed inner- and outer-halo posterior probabilities are forced to unity at each point, the two curves simply complement one another.

The values obtained for the mean rotational velocity and its dispersion are, for the inner halo,  $V_{\phi} = 56 \pm 11 \text{ km s}^{-1}$ , and  $\sigma_{V_{\phi}} = 93 \pm 35 \text{ km s}^{-1}$ ; for the outer halo,  $V_{\phi} = -141 \pm$

$31 \text{ km s}^{-1}$ , and  $\sigma_{V_{\phi}} = 138 \pm 58 \text{ km s}^{-1}$ . The errors on the velocity and its dispersion have been evaluated by employing the jackknife method. A K-S test of the null hypothesis that the velocity distributions of stars belonging to the inner- and outer-halo components could be drawn from the same parent population is rejected at a high level of statistical significance ( $p < 0.001$ ).

#### 4.5. Contrast of CEMP Stellar Fractions in the Two Halo Components

We now consider the distribution of carbonicity ( $[\text{C}/\text{Fe}]$ ) for the Extended Sample with metallicity  $[\text{Fe}/\text{H}] < -2.0$  and at  $Z_{\text{max}} > 5$  kpc. These selections ensure the presence of essentially all halo stars in the sample, with little or no contamination expected from the thick disk or MWTD. The top panel of Figure 14 shows the CarDF for the Extended Sample<sup>7</sup>. There are two clear peaks that emerge, one at  $[\text{C}/\text{Fe}] \sim +0.3$  to  $+0.5$ , and the second softer peak around  $[\text{C}/\text{Fe}] \sim +1.8$ , along with a tail extending towards higher values of carbonicity. The bottom panel of Figure 14 shows the weighted CarDFs for the inner- and outer-halo components. The underlying distribution of each population has been obtained by weighting the values of the CarDF with the membership probabilities of each star. As usual, the green distribution denotes the inner halo, while the red distribution represents the outer halo. A K-S test of the null hypothesis that the CarDF of stars belonging to the inner- and outer-halo components could be drawn from the same parent population is rejected at high statistical significance ( $p < 0.001$ ), clearly indicating that the carbonicity distribution functions of the inner- and outer-halo components are distinct.

The contrast of the CEMP star fractions in the inner- and outer-halo components can be investigated by applying the XD analysis to subsamples of stars in restricted ranges of metallicity. The stars employed are those belonging to the Extended Sample, selected in the low metallicity range ( $[\text{Fe}/\text{H}] < -1.5$ ) and with  $Z_{\text{max}} > 5$  kpc.

A first attempt was made by selecting stars in intervals of metallicity such that  $\Delta[\text{Fe}/\text{H}] = 0.2$  dex, and applying the XD technique to the rotational velocity distribution of each subsample. This experiment was not successful, due to the low number of stars in each bin. A much better result has been obtained by choosing a larger interval on metallicity,  $\Delta[\text{Fe}/\text{H}] = 0.5$  dex.

The left panel of Figure 15 shows the previously determined global trend of the CEMP star fraction, as a function of metallicity (dashed curve), overplotted with the derived inner- and outer-halo CEMP star fractions. The blue filled stars represent the predicted values of the CEMP star fractions for each bin of metallicity, i.e.,  $-2.0 < [\text{Fe}/\text{H}] < -1.5$ ,  $-2.5 < [\text{Fe}/\text{H}] < -2.0$ , and  $-3.0 < [\text{Fe}/\text{H}] < -2.5$  (hereafter bin1, bin2, and bin3). The predicted values are derived using the global trend of CEMP star fractions vs.  $[\text{Fe}/\text{H}]$  (second-order polynomial; Fig. 11), and the posterior probability for each star in the subsamples associated with each bin of metallicity, such that:

$$F_{\text{CEMP}_{\text{pred}}}^k = \frac{1}{\sum_i (p_{ij})} \cdot \sum_i (p_{ij} f^k) \quad (13)$$

where  $p_{ij}$  is the posterior probability, derived by applying

<sup>7</sup> Note that the number of stars shown in Figure 14 differs from the numbers shown in Figure 13, as Figure 14 includes only stars with detected CH G-band features.

the XD analysis to the subsample of stars selected in bin1, bin2, and bin3, respectively. The parameter  $f^k$  represents the CEMP star fractions obtained in each bin of metallicity from application of the second order polynomial ( $j$  and  $k$  denote the halo component and the bin of metallicity, respectively).

Note that the expression in Eqn. 13 provides an estimate of the CEMP fraction that is driven by the global trend of  $F_{CEMP}$  as a function of the metallicity (Fig. 11, left panel). Eqn. 13 makes use of the full shape of the posterior probability, and thus, a considerable overlap between the kinematic distributions of the two components is still present. Therefore, we are not expecting to find a significant difference in the predicted values for the two components in each bin of  $[\text{Fe}/\text{H}]$ .

The predicted value of CEMP star fractions in bin1 is  $F_{CEMP_{pred, in, 1}} = (5.8 \pm 0.03)\%$ ,  $F_{CEMP_{pred, out, 1}} = (5.9 \pm 0.03)\%$ , for the inner halo and outer halo, respectively. The same calculations for bin2 provide  $F_{CEMP_{pred, in, 2}} = (11.9 \pm 0.1)\%$  and  $F_{CEMP_{pred, out, 2}} = (12.0 \pm 0.1)\%$ . For the third bin we find  $F_{CEMP_{pred, in, 3}} = (22.9 \pm 0.6)\%$  and  $F_{CEMP_{pred, out, 3}} = (22.7 \pm 0.6)\%$ . The error on each fraction is evaluated by employing the jack-knife method. These fractions are sufficiently close to one another that only a single set of blue stars is shown in the left panel of Figure 15 to represent both results.

Not surprisingly, the above predicted values of the CEMP star fractions in the inner and outer halo are very similar in all bins of metallicity. The presence of a contrast in the CEMP star fraction for the two components can be better investigated by reducing the overlap in the kinematic distributions. This can be done by employing the *hard-cut-in-probability* method. For each halo component, the lower limit of the membership probability is chosen to be  $p_{lim} = 0.7$ . This limit is set reasonably high to reduce the contamination between the halo components. We have selected two subsamples of stars such that  $p_{i, inner} > p_{lim}$ , and  $p_{i, outer} > p_{lim}$  ( $i$  denotes the star), and for each subsample, the CEMP star fraction is evaluated following Eqn. 2.

The result of this exercise is shown in the left panel of Figure 15. Here, the green (inner) and the red (outer) filled circles denote the values of the CEMP star fractions obtained by employing the hard-cut-in-probability method. The observed CEMP star fractions in bin1 are  $F_{CEMP_{obs, in, 1}} = (5.2 \pm 0.6)\%$  and  $F_{CEMP_{obs, out, 1}} = (7.7 \pm 1.0)\%$ , for the inner and outer halo, respectively. In the case of bin2, we find  $F_{CEMP_{obs, in, 2}} = (9.4 \pm 0.8)\%$  and  $F_{CEMP_{obs, out, 2}} = (20.3 \pm 2.3)\%$ . Finally, in the third bin, the observed fractions are  $F_{CEMP_{obs, in, 3}} = (20.5 \pm 2.4)\%$  and  $F_{CEMP_{obs, out, 3}} = (30.4 \pm 4.8)\%$ .

In the highest metallicity bin,  $-2.0 < [\text{Fe}/\text{H}] < -1.5$ , the CEMP star fractions for the two halo components are close to the expected value ( $\sim 6\%$ ), with overlapping error bars. Note that the inner halo is the dominant component in this range of metallicity ( $[\text{Fe}/\text{H}]_{peak, in} = -1.6$ ), and we were not expecting to find a high contrast in the CEMP star fractions. At lower metallicity,  $-2.5 < [\text{Fe}/\text{H}] < -2.0$ , where the dominant component is the outer halo ( $[\text{Fe}/\text{H}]_{peak, out} = -2.2$ ), there is evidence of a significant contrast in CEMP fractions between the inner- and outer-halo components, such that  $F_{CEMP_{obs, out, 2}} \sim 2 \times F_{CEMP_{obs, in, 2}}$ . This contrast is confirmed also in the lowest bin of metallicity,  $-3.0 < [\text{Fe}/\text{H}] < -2.5$ , even though it is less remarkable,  $F_{CEMP_{obs, out, 3}} \sim 1.5 \times F_{CEMP_{obs, in, 3}}$ , and has a much larger error bar, due to the smaller numbers of stars involved.

It is important to note that most of the stars in the lowest metallicity bin belong to the category for which only an up-

per limit of  $[\text{C}/\text{Fe}]$  has been provided (classified as subsample L, see Section 2.4). A significant number of stars in the lowest metallicity bin have high  $T_{eff}$  ( $\sim 65\%$  above 6250 K), and thus only quite high values of  $[\text{C}/\text{Fe}]$  are expected to be detected. Thus, it is our expectation that the quoted frequencies for CEMP star fractions, at least at low metallicity, represent lower limits. Moreover, the SDSS/SEGUE DR7 calibration-star sample has a limited number of stars with  $[\text{Fe}/\text{H}] < -2.5$ . The extremely metal-poor regime will be further investigated in a future paper using the much larger sample of such stars in the SDSS/SEGUE DR8 release (Aihara et al. 2011).

Interestingly, the right panel of Figure 15 shows that the mean carbonicity,  $\langle [\text{C}/\text{Fe}] \rangle$ , remains similar for both the inner- and outer-halo components as a function of declining metallicity. There is a hint of a split emerging for the lowest metallicity bin,  $-3.0 < [\text{Fe}/\text{H}] < -2.5$ , with the outer-halo  $\langle [\text{C}/\text{Fe}] \rangle$  being slightly higher than that of the inner-halo value. However, the error bars overlap, indicating that the sample size is simply too small to be certain.

## 5. SUMMARY AND DISCUSSION

We have analyzed the SDSS/SEGUE DR7 calibration stars in order to explore the global properties of the carbonicity distribution function ( $[\text{C}/\text{Fe}]$ ; CarDF) of the halo components of the Milky Way, and the possible contrast of the CEMP star fractions and mean carbonicity between the inner halo and the outer halo. Carbon-to-iron abundance ratios (or limits) have been obtained for 31187 stars, based on matches to a grid of synthetic spectra to the CH G-band at 4305 Å, with an external error for  $[\text{C}/\text{Fe}]$  on the order of 0.25 dex. Kinematic and orbital parameters were derived employing the methodologies described in C10. We have considered the nature of the samples of stars considered CEMP ( $[\text{C}/\text{Fe}] > +0.7$ ) and non-CEMP ( $[\text{C}/\text{Fe}] < +0.7$ ), and shown that, at low metallicity ( $[\text{Fe}/\text{H}] < -1.5$ ), their distributions on distance and rotational velocity differ significantly from one another. For the stars with a detectable CH G-band, a deconvolution of the inner- and outer-halo components, along with a derivation of the membership probabilities, has been obtained by applying the Extreme Deconvolution (XD) analysis to the Extended Sample of calibration stars, selected in the low metallicity range ( $[\text{Fe}/\text{H}] < -1.5$ ) and with  $Z_{max} > 5$  kpc. Contrasts of the CEMP star fractions and mean carbonicity have been obtained by employing the hard-cut-in-probability method to subsamples of stars selected in several bins of metallicity.

### 5.1. Summary of Main Results

Our main results are the following:

- The as-observed distribution of  $[\text{C}/\text{Fe}]$ , which we refer to as the carbonicity distribution function (CarDF), has been derived at various intervals on distance above or below the Galactic plane. At  $|Z| > 5$  kpc, where we expect to see the beginning of the transition from inner-halo dominance to outer-halo dominance among halo stars, the CarDF exhibits a strong peak at  $[\text{C}/\text{Fe}] \sim +0.3$ , and a long tail towards high values of carbonicity, up to  $[\text{C}/\text{Fe}] = +3.0$ . The fraction of CEMP stars (defined here to mean  $[\text{C}/\text{Fe}] > +0.7$ ) for the subsample at  $|Z| > 9$  kpc (where the dominant component is the outer halo) is 20%, in agreement with several previous estimates for stars at similarly very low metallicities,  $[\text{Fe}/\text{H}] < -2.0$ .

- At low metallicities ( $[\text{Fe}/\text{H}] < -1.5$ ), the distribution of derived distances and rotational velocities for the CEMP and non-CEMP stars differ significantly from one another.
- *Almost all* of the CEMP stars are located in the halo components of the Milky Way.
- We observe a significant increase of the fraction of CEMP stars with declining metallicity in the halo system. Following Eqn. 2, we find that 2%, 7%, and 20% of stars in the metallicity intervals  $-1.5 < [\text{Fe}/\text{H}] < -0.5$ ,  $-2.5 < [\text{Fe}/\text{H}] < -1.5$ , and  $[\text{Fe}/\text{H}] < -2.5$ , are carbon-rich, respectively. For ease of comparison with previous estimates, the global frequency of CEMP stars in the halo system for  $[\text{Fe}/\text{H}] < -1.5$  is 8%; for  $[\text{Fe}/\text{H}] < -2.0$  it is 12%; for  $[\text{Fe}/\text{H}] < -2.5$  it is 20%. For reasons described above, we believe these fractions should be considered lower limits.
- In the low-metallicity regime ( $[\text{Fe}/\text{H}] < -1.5$ ), and at vertical distances  $Z_{\text{max}} > 5$  kpc, a continued increase of the fraction of CEMP stars with declining metallicity is found (Fig. 11, left panel). A second-order polynomial provides a good fit to the CEMP star fraction as a function of  $[\text{Fe}/\text{H}]$ .
- In the same metallicity regime the mean carbonicity,  $\langle [\text{C}/\text{Fe}] \rangle$ , increases with declining metallicity (Fig. 11, right panel).
- In the low-metallicity regime, for both  $-2.0 < [\text{Fe}/\text{H}] < -1.5$  and  $[\text{Fe}/\text{H}] < -2.0$ , we find a clear increase in the CEMP star fraction with distance from the Galactic plane,  $|Z|$  (Fig. 12). At these low metallicities, significant contamination from the thick disk and MWTD populations is unlikely, and would only have a small effect for the bin with  $0 \text{ kpc} < |Z| < 4 \text{ kpc}$  and  $-2.0 < [\text{Fe}/\text{H}] < -1.5$ ; this is an observed property of the halo system. The mean carbonicity remains roughly constant as a function of  $|Z|$ , taking a value of  $\langle [\text{C}/\text{Fe}] \rangle \sim +1.0$  for  $-2.0 < [\text{Fe}/\text{H}] < -1.5$ , and  $\langle [\text{C}/\text{Fe}] \rangle \sim +1.5$  for  $[\text{Fe}/\text{H}] < -2.0$ .
- The Extreme Deconvolution technique of BHR11 has been applied to subsamples of stars selected in three bins of metallicity,  $-2.0 < [\text{Fe}/\text{H}] < -1.5$ ,  $-2.5 < [\text{Fe}/\text{H}] < -2.0$ , and  $-3.0 < [\text{Fe}/\text{H}] < -2.5$ , and with  $Z_{\text{max}} > 5$  kpc. We have successfully decomposed the inner and outer halo in all three bins, and obtained the inner- and outer-halo membership probabilities for each star.
- At low metallicity,  $-2.0 < [\text{Fe}/\text{H}] < -1.5$ , where the dominant component is the inner halo ( $[\text{Fe}/\text{H}]_{\text{peak, in}} = -1.6$ ), there is no significant difference in the CEMP star fraction between the inner and outer halo. In contrast, at very low metallicity,  $-2.5 < [\text{Fe}/\text{H}] < -2.0$ , where the dominant component is the outer halo ( $[\text{Fe}/\text{H}]_{\text{peak, out}} = -2.2$ ), there is evidence for a significant difference in the CEMP star fraction between the inner and the outer halo (Figure 15, left panel), such that  $F_{\text{CEMP, obs, out, 2}} \sim 2 \times F_{\text{CEMP, obs, in, 2}}$ . This difference is also confirmed in the lowest metallicity bin,  $-3.0 < [\text{Fe}/\text{H}] < -2.5$ , even though it is less remarkable,  $F_{\text{CEMP, obs, out, 3}}$

$\sim 1.5 \times F_{\text{CEMP, obs, in, 3}}$ , and has a larger error bar. We conclude that the difference in CEMP frequency at very low metallicity is not driven by metallicity itself, but rather, by the stellar populations present.

- The mean carbonicity,  $\langle [\text{C}/\text{Fe}] \rangle$ , remains similar for both the deconvolved inner- and outer-halo components as a function of declining metallicity. Larger samples of low-metallicity CEMP stars are required to see if a split in mean carbonicity emerges.

## 5.2. Implications for Galaxy Formation

A possible scenario for the formation of the inner- and the outer-halo components has been described in C07. The fact that the outer-halo component of the Milky Way exhibits a net retrograde rotation (and a different distribution of overall orbital properties), clearly indicates that the formation of the outer halo is distinct from that of the inner halo and the disk components. In C07, it was suggested that the outer-halo component formed, not through a dissipational, angular-momentum conserving contraction, but rather through dissipationless chaotic merging of smaller subsystems within a pre-existing dark matter halo. These subsystems would be expected to be of much lower mass, and subject to tidal disruption in the outer part of a dark matter halo, before they fall farther into the inner part. As candidate (surviving) counterparts for such subsystems, one might consider the low luminosity dwarf spheroidal galaxies surrounding the Milky Way. In the case of the inner halo, C07 argued that the low-mass sub-Galactic fragments, formed at an early stage, rapidly merge into several more massive clumps, which themselves eventually dissipationally merge (owing to the presence of gas that had yet to form stars). The essentially radial merger of the few resulting massive clumps gives rise to the dominance of high-eccentricity orbits for stars that we assign to membership in the inner halo. Star formation within these massive clumps (both pre- and post-merger) would drive the mean metallicity to higher abundances. This would be followed by a stage of adiabatic compression (flattening) of the inner-halo component owing to the growth of a massive disk, along with the continued accretion of the gas onto the Galaxy. This general picture is supported, at least qualitatively, by the most recent numerical simulations of the formation and evolution of large disk galaxies that include prescriptions to handle the presence of gas, and which also include approximate star-formation schemes and follow the evolving chemistry (e.g., Zolotov et al. 2010; Font et al. 2011; McCarthy et al. 2011; Tissera et al. 2011).

The large fractions of CEMP stars in both halo components indicates that significant amounts of carbon were produced in the early stages of chemical evolution in the universe. The observed contrast of CEMP star fractions between the inner halo and outer halo strengthen the picture that the halo components had different origins, and supports a scenario in which the outer-halo component has been assembled by the accretion of small subsystems, as discussed below. In this regard, it is interesting that the MDF of the inner halo (peak metallicity at  $[\text{Fe}/\text{H}] \sim -1.6$ ) is in the metallicity regime associated with the CEMP-s stars, which are primarily found with  $[\text{Fe}/\text{H}] > -2.5$ , while the MDF of the outer halo (metallicity peak at  $[\text{Fe}/\text{H}] \sim -2.2$ ) might be associated with the metallicity regime of the CEMP-no stars, which are primarily found with  $[\text{Fe}/\text{H}] < -2.5$  (Aoki et al. 2007b).

The fact that, in the metal-poor regime, the outer halo ex-



hibits a fraction of CEMP stars that is larger than the inner halo ( $\text{CEMP}_{\text{outer}} \sim 2 \cdot \text{CEMP}_{\text{inner}}$ ), suggests that multiple sources of carbon, besides the nucleosynthesis of AGB stars in binary systems, were present in the pristine environment of the outer-halo progenitors (lower mass sub-halos). These sources could be the fast massive rotators and/or the faint supernovae mentioned in the Introduction. Karlsson (2006) also explored the possibility that primordial gas was pre-enriched in heavy metals by less massive SNe ( $13 < M/M_{\odot} < 30$ ), whose ejecta underwent substantial mixing and fall-back, while the C (and N, O) originated from massive rotating stars with  $M \geq 40 M_{\odot}$ . If the CEMP stars in the outer halo are predominantly CEMP-no stars (which has yet to be established), it might suggest that non-AGB-related carbon production took place in the primordial mini-halos. The predominance of CEMP-s stars in the inner halo, if found, would suggest that the dominant source of carbon was the nucleosynthesis by AGB stars in binary systems. This would place important constraints on the primordial IMF of the sub-systems responsible for the formation of the two halo components.

Recent efforts to model, from the population synthesis standpoint, the fractions of observed CEMP stars in the halo have not managed to reproduce results as high as 15-20% for metallicities  $[\text{Fe}/\text{H}] < -2.0$  (e.g., Izzard et al. 2009; Pols et al. 2010). However, these predictions are based solely on carbon production by AGB stars. While such calculations may prove meaningful for the inner-halo population, they may not be telling the full story for carbon production associated with the progenitors of the outer-halo population. Indeed, the observed increase of the CEMP star fraction with  $|Z|$  (in particular, far from the Galactic plane) we have found would be difficult to understand if the halo system represents a single population. In any event, the lower CEMP fraction in the inner halo may relieve some of the tension with current model predictions.

The fact that the CEMP star fraction exhibits a clear increase with  $|Z|$  suggests that the relative numbers of CEMP stars in a stellar population is not driven by metallicity alone. The proposed coupling of the cosmic microwave background to the initial mass function (CMB-IMF hypothesis; Larson 1998, 2005; Tumlinson 2007) is one mechanism for imposing a temporal dependence on the IMF. This effect, coupled with chemical evolution models, predicts that the CEMP fraction would be expected to increase as the metallicity decreases, but with similar metallicity regimes forming carbon according to the expected yields of the predominant mass range available at that time. In the hierarchical context of galaxy formation,

star-forming regions are spatially segregated, and their chemical evolution can proceed at different rates, with stars at the same metallicity forming at different times. Depending on the source(s) of carbon, this trend could lead to a spatial variation of the CEMP fraction at the same metallicity, increasing in older populations and decreasing in younger ones.

The larger fraction of CEMP stars associated with the outer-halo component could be due to the nature of the progenitor low-mass mini-halos (mass, density, etc.) in which they formed. A natural place to look for surviving examples are the ultra-faint dwarf spheroidal galaxies surrounding the Milky Way discovered in the course of the SDSS (Willman et al. 2005; Belokurov et al. 2006a,b; Zucker et al. 2006, and many others since). Early hints of the possible association of CEMP stars with the ultra-faint galaxies came from the recognition that a (serendipitously) spectroscopically targeted star from SDSS in the direction of the Canes Venatici ultra-faint dwarf, SDSS J1327+3335, is a carbon-rich giant with a radial velocity and inferred distance commensurate with this very metal-poor satellite galaxy (Zucker et al. 2006). The existence of CEMP stars in ultra-faint dwarf spheroidal galaxies has now been definitively established (Norris et al. 2010a,b; Lai et al. 2011). Norris et al. 2010b reported the discovery of an extremely carbon-rich red giant, Segue 1-7, in the Segue 1 system. This star exhibits a metallicity  $[\text{Fe}/\text{H}] = -3.5$ , carbonicity  $[\text{C}/\text{Fe}] = +2.3$ , and a low barium abundance ratio ( $[\text{Ba}/\text{Fe}] < -1.0$ ), which place it in the CEMP-no category. This discovery is consistent with the idea that the CEMP-no stars may indeed be associated with the ultra-faint dwarf spheroidal galaxies; further similar investigations should prove of great interest.

D.C. gratefully acknowledges funding from RSAA ANU to pursue her research. T.C.B. and Y.S.L. acknowledge partial funding of this work from grants PHY 02-16783 and PHY 08-22648: Physics Frontier Center/Joint Institute for Nuclear Astrophysics (JINA), awarded by the U.S. National Science Foundation. J.B. was partially supported by NASA (grant NNX08AJ48G) and the NSF (grant AST 09-08357). Studies at ANU of the most metal-poor populations of the Milky Way are supported by Australian Research Council grants DP0663562 and DP0984924, which are gratefully acknowledged by J. E. N. and D. C.

*Facilities:* SDSS.

## REFERENCES

- Abazajian, K., et al. 2009, *ApJS*, 182, 543  
 Aihara, H., et al. 2011, *ApJS*, 193, 29  
 Allende Prieto, C., et al. 2008, *AJ*, 136, 2070  
 Alvarez, R., & Plez, B. 1998, *A&A*, 330, 1109  
 Aoki, W., et al. 2007a, *ApJ*, 660, 747  
 Aoki, W., Beers, T. C., Christlieb, N., Norris, J. E., Ryan, S. G., & Tsangarides, S. 2007b, *ApJ*, 655, 492  
 Aoki, W., et al. 2008, *ApJ*, 678, 1351  
 Aoki, W., Beers, T. C., Honda, S., & Carollo, D. 2010, *ApJ*, 723, L201  
 Asplund, M., Grevesse, N., & Sauval, A. J. 2005, in *Cosmic Abundances as Records of Stellar Evolution and Nucleosynthesis in Honor of David L. Lambert*, ASP Conf. Ser. 336, p. 25  
 Barklem, P. S., & O'Mara, B. J. 1998, *MNRAS*, 300, 863  
 Barklem, P. S., & Asplund, M. 2005, *A&A*, 435, 373  
 Beers, T. C., Preston, G. W., & Shectman, S. A., 1985, *AJ*, 90, 2089  
 Beers, T. C., Preston, G. W., & Shectman, S. A., 1992, *AJ*, 103, 1987  
 Beers, T. C., Rossi, S., Norris, J. E., Ryan, S. G., & Shefler, T. 1999, *AJ*, 117, 981  
 Beers, T. C., Chiba, M., Yoshii, Y., Platais, I., Hanson, R. B., Fuchs, B., & Rossi, S. 2000, *AJ*, 119, 2866  
 Beers, T. C. & Christlieb, N. 2005, *ARA&A*, 43, 531  
 Beers, T. C., Sivarani, T., Marsteller, B., Lee, Y. S., Rossi, S., & Plez, B. 2007, *AJ*, 133, 1193  
 Beers, T. C., et al. 2011, *ApJ*, submitted (arXiv:1104.2513)  
 Behara, N. T., Bonifacio, P., Ludwig, H.-G., Sbordone, L., Gonzalez Hernandez, J. I., & Caffau, E. 2010, *A&A*, 513, 72  
 Belokurov, V., et al. 2006a, *ApJ*, 642, L137  
 Belokurov, V., et al. 2006b, *ApJ*, 647, L111  
 Bisterzo, S., Gallino, R., Straniero, O., Cristallo, S., & Käppeler, F. 2011, *MNRAS*, in press (arXiv:1108.0500)  
 Bovy, J., Hogg, D. W., & Roweis, S. T. 2011, *Annals of Applied Statistics*, 5, No. 2, 1657 (arXiv:0905.2979) (BHR11)  
 Bullock, J. S., & Johnston, K. V. 2005, *ApJ*, 635, 931  
 Caffau, E., et al. 2011, *Nature*, 477, 67  
 Carollo, D., et al. 2007, *Nature*, 450, 1020 (C07)  
 Carollo, D., et al. 2010, *ApJ*, 712, 692 (C10)

- Castelli, F. & Kuruz, R. L. 2003, *Modelling of Stellar Atmospheres*, Proceedings of the 210th Symposium of the International Astronomical Union, 210, A20
- Christlieb, N., et al. 2002, *Nature*, 419, 904
- Christlieb, N. 2003, *Reviews in Modern Astronomy*, 16, 191
- Cohen, J. G., et al. 2005, *ApJ*, 633, L109
- Cohen, J. G., McWilliam, A., Christlieb, N., Shectman, S. A., Thompson, I., Melendez, J., Wisotzki, L., & Reimers, D. 2007, *ApJ*, 659, L161
- Cooke, R., Pettini, M., Steidel, C. C., Rudie, G. C., & Jorgenson, R. A. 2011, *MNRAS*, 412, 1047
- Cottrell, P. L., & Norris, J. 1978, *ApJ*, 221, 893
- de Jong, J. T. A., Yanny, B., Rix, H. -W., Dolphin, A. E., Martin, N. F., & Beers, T. C. 2010, *ApJ*, 714, 663
- Dempster, A. P., Laird, N. M., & Rubin, D. B. 1977, *Journ. Roy. Stat. Soc.*, 39, 1
- Font, A. S., McCarthy, I. G., Crain, R. A., Theuns, T., Schaye, J., Wiersma, R. P. C., & Dalla Vecchia, C. 2011, *MNRAS*, in press (arXiv:1102.2526)
- Frebel, A., et al. 2005, *Nature*, 434, 871
- Frebel, A., et al. 2006, *ApJ*, 652, 1585
- Frebel, A., Kirby, E. N., & Simon, J. D. 2010, *Nature*, 464, 72
- Gunn, J. E., et al. 2006, *AJ*, 131, 2332
- Herwig, F. 2005, *ARA&A*, 43, 435
- Hirschi, R., Frölich, C., Liebrandt, M., & Thieleman, F. -K. 2006, *Reviews in Modern Astronomy*, 19, 101
- Ito, H., Aoki, W., Honda, S., & Beers, T. C. 2009, *ApJ*, 698, L37
- Ivezić, Ž., et al. 2008, *ApJ*, 684, 287
- Izzard, R. G., Glebbeek, E., Stancliffe, R. J., & Pols, O. 2009, *PASA*, 26, 311
- Karlsson, T. 2006, *ApJ*, 641, L41
- Kennedy, C. R., Sivarani, T., Beers, T. C., Lee, Y. S., Placco, V. M., Rossi, S., Christlieb, N., Herwig, F., & Plez, B. 2011, *AJ*, 141, 102
- Kobayashi, C., Tominaga, N., & Nomoto, K. 2011, *ApJ*, 730, L14
- Lai, D. K., Rockosi, C. M., Bolte, M., Johnson, J. A., Beers, T. C., Lee, Y. S., Allende Prieto, C., & Yanny, B. 2009, *ApJ*, 697, L63
- Lai, D. K., Lee, Y. S., Bolte, M., Lucatello, S., Beers, T. C., Johnson, J. A., Sivarani, T., & Rockosi, C. M. 2011, *ApJ*, 738, 51
- Larson, R. B. 1998, *MNRAS*, 301, 569
- Larson, R. B. 2005, *MNRAS*, 359, 211
- Lee, Y. S., et al. 2008a, *AJ*, 136, 2022
- Lee, Y. S., et al. 2008b, *AJ*, 136, 2050
- Lee, Y. S., et al. 2011, *AJ*, 141, 90
- Lucatello, S., Beers, T. C., Christlieb, N., Barklem, P. S., Rossi, S., Marsteller, B., Sivarani, T., & Lee, Y. S. 2006, *ApJ*, 652, L37
- Marsteller, B., Beers, T. C., Rossi, S., Christlieb, N., Bessell, M., & Rhee, J. 2005, *Nucl. Phys. A*, 758, 312
- Matsuoka, K., Nagao, T., Maiolino, R., Marconi, A., & Taniguchi, Y. 2011, *A&A*, 532, L10
- Masseron, T., Plez, B., Primas, F., Van Eck, S., & Jorissen, A. 2005, in *From Lithium to Uranium: Elemental Tracers of Early Cosmic Evolution*, IAU Symposium 228, p. 219
- McCarthy, I. G., Font, A. S., Crain, R. A., Schaye, J., Theuns, T., & Deason, A. J. 2011, *MNRAS*, submitted
- Meynet, G., Ekström, S., & Maeder, A. 2006, *A&A*, 447, 623
- Meynet, G., Hirschi, R., Ekström, S., Maeder, A., Georgy, C., Eggenberger, P., & Chiappini, C. 2010a, in *Chemical Abundances in the Universe: Connecting First Stars to Planets*, IAU Symposium 265, p. 98
- Meynet, G., Hirschi, R., Ekström, S., Maeder, A., Georgy, C., Eggenberger, P., & Chiappini, C. 2010b, *A&A*, 521
- Nissen, P. E., & Schuster, W. J. 2010, *A&A*, 511, L10
- Norris, J. E., Christlieb, N., Korn, A. J., Eriksson, K., Bessell, M. S., Beers, T. C., Wisotzki, L., & Reimers, D. 2007, *ApJ*, 670, 774
- Norris, J. E., Yong, D., Gilmore, G., & Wyse, R. F. G. 2010a, *ApJ*, 711, 350
- Norris, J. E., Gilmore, G., Wyse, R. F. G., Yong, D., & Frebel, A. 2010b, *ApJ*, 722, L104
- Norris, J. E., Wyse, R. F. G., Gilmore, G., Yong, D., Frebel, A., Wilkinson, M. L., Belokurov, V., & Zucker, D. B. 2010c, *ApJ*, 723, 1632
- Plez, B., & Cohen, J. G. 2005, *A&A*, 434, 1117
- Pols, O. R., Izzard, R. G., Glebbeek, E., & Stancliffe, R. J. 2010, in *Chemical Abundances in the Universe: Connecting First Stars to Planets*, IAU Symposium, Vol. 265, p. 117
- Roeederer, I. U., 2009, *ApJ*, 137, 272
- Rossi, S., Beers, T. C., Sneden, C., Sevastyanenko, T., Rhee, J., & Marsteller, B. 2005, *AJ*, 130, 2804
- Schlaufman, K. C., et al. 2009, *ApJ*, 703, 2177
- Schlaufman, K. C., Rockosi, C. M., Lee, Y. S., Beers, T. S., & Allende Prieto, C. 2011, *ApJ*, 734, 49
- Schlegel, D. J., Finkbeiner, D. P., & Davis, M. 1998, *ApJ*, 500, 525
- Schönrich, R., Asplund, M., & Casagrande, L. 2011, *MNRAS*, 415, 3807
- Sivarani, T., et al. 2006, *A&A*, 459, 125
- Smolinski, J. P., et al. 2011, *AJ*, 141, 89
- Sneden, C., Cowan, J. J., & Gallino, R. 2008, *ARA&A*, 46, 241
- Tissera, P. B., White, S. D. M., & Scannapieco, C. 2011, *MNRAS*, submitted
- Tominaga, N., Umeda, H., & Nomoto, K. 2007, *ApJ*, 660, 516
- Tumlinson, J. 2007, *ApJ*, 664, L63
- Tumlinson, J. 2010, *ApJ*, 708, 1398
- Umeda, H. & Nomoto, K. 2003, *Nature*, 422, 871
- Umeda, H. & Nomoto, K. 2005, *ApJ*, 619, 427
- Willman, B., et al. 2005, *ApJ*, 626, L85
- Wall, J. V., & Jenkins, C. R. 2003, *Practical Statistics for Astronomers*, (Cambridge University Press, Cambridge)
- Wisotzki, L., Christlieb, N., Bade, N., Beckmann, V., Köhler, T., Vanelle, C., & Reimers, D. 2000, *A&A*, 358, 77
- Yanny, B., et al. 2009, *AJ*, 137, 4377
- York, D. G., et al. 2000, *AJ*, 120, 1579
- Zolotov, A., Willman, B., Brooks, A. M., Governato, F., Hogg, D. W., Shen, S., & Wadley, J. 2010, *ApJ*, 721, 738
- Zucker, D. B., et al. 2006, *ApJ*, 643, L103

TABLE 1  
COMPARISON WITH HIGH-RESOLUTION SPECTROSCOPY:  
ATMOSPHERIC PARAMETERS AND [C/Fe] DETERMINATIONS

IAU Name	PLATE-MJD-FIBER	REF	$T_{\text{eff}}$ HIGH	$T_{\text{eff}}$ SSPP	log $g$ HIGH	log $g$ SSPP	[Fe/H] HIGH	[Fe/H] SSPP	[C/Fe] HIGH	[C/Fe] SSPP
SDSS J000219.9+292851.8	2803-54368-459	A11	6150	6184	4.00	3.24	-3.26	-2.97	+2.63	+2.73
SDSS J003602.2-104336.3	<sup>a</sup> 0654-52146-011	A08	6500	6475	4.50	4.59	-2.41	-2.49	+2.50	+2.21
SDSS J012617.9+060724.8	2314-53713-090	A08	6600	6841	4.10	4.73	-3.11	-2.80	+2.92	+2.67
SDSS J012617.9+060724.8	2314-53713-090	A11	6900	6841	4.00	4.73	-3.01	-2.80	+3.08	+2.67
SDSS J025956.4+005713.3	1513-53741-338	A11	4550	4537	5.00	4.31	-3.31	-3.75	-0.02	+0.00
SDSS J030839.3+050534.9	2335-53730-314	A11	5950	5938	4.00	3.36	-2.19	-2.41	+2.36	+2.31
SDSS J035111.3+102643.2	2679-54368-543	A11	5450	5542	3.60	3.14	-3.18	-2.89	+1.55	+1.61
SDSS J071105.4+670128.2	2337-53740-564	A11	5350	5252	3.00	2.70	-2.91	-2.91	+1.98	+2.16
SDSS J072352.2+363757.2	2941-54507-222	A11	5150	5105	2.20	2.33	-3.32	-3.48	+1.79	+1.39
SDSS J074104.2+670801.8	2939-54515-414	A11	5200	5171	2.50	2.35	-2.87	-2.92	+0.74	+0.84
SDSS J081754.9+264103.8	<sup>a</sup> 1266-52709-432	A08	6300	6075	4.00	3.58	-3.16	-3.03	< +2.20	< +1.54
SDSS J081754.9+264103.8	<sup>a</sup> 1266-52709-432	A11	6050	6075	4.00	3.58	-2.85	-3.03	...	< +1.54
SDSS J091243.7+021623.7	<sup>a</sup> 0471-51924-613	A11	6150	6138	4.00	3.40	-2.68	-2.76	+2.05	+2.33
SDSS J091243.7+021623.7	<sup>a</sup> 0471-51924-613	B10	6500	6138	4.50	3.40	-2.50	-2.76	+2.17	+2.33
SDSS J092401.9+405928.7	<sup>a</sup> 0938-52708-608	A08	6200	6201	4.00	4.53	-2.51	-2.81	+2.72	+2.56
SDSS J103649.9+121219.8	<sup>a</sup> 1600-53090-378	B10	6000	5873	4.00	3.12	-3.20	-3.31	+1.47	+1.94
SDSS J124123.9-083725.5	2689-54149-292	A11	5150	5108	2.50	2.45	-2.73	-2.90	+0.50	+0.65
SDSS J124204.4-033618.1	2897-54585-210	A11	5150	5112	2.50	2.56	-2.77	-3.02	+0.64	+0.77
SDSS J134913.5-022942.8	<sup>a</sup> 0913-52433-073	A11	6200	6167	4.00	4.39	-3.24	-3.16	+3.01	+2.61
SDSS J134913.5-022942.8	<sup>a</sup> 0913-52433-073	B10	6200	6167	4.00	4.39	-3.00	-3.16	+2.82	+2.61
SDSS J161226.2+042146.6	2178-54629-546	A11	5350	5365	3.30	2.42	-2.86	-3.19	+0.63	+0.98
SDSS J161313.5+530909.7	2176-54243-614	A11	5350	5338	1.60	2.67	-3.32	-2.89	+2.09	+1.64
SDSS J164610.2+282422.2	<sup>a</sup> 1690-53475-323	A11	6100	6125	4.00	3.45	-3.05	-2.78	+2.52	+2.53
SDSS J170339.6+283649.9	2808-54524-510	A11	5100	5120	4.80	3.58	-3.21	-3.32	+0.28	+0.43
SDSS J170733.9+585059.7	0353-51703-195	A08	6700	6567	4.20	3.47	-2.52	-2.68	+2.10	+2.43
SDSS J173417.9+431606.5	2799-54368-138	A11	5200	5172	2.70	2.15	-2.51	-3.18	+1.78	+2.43
SDSS J204728.8+001553.8	<sup>a</sup> 0982-52466-480	A08	6600	6324	4.50	3.77	-2.05	-2.28	+2.00	+1.98

NOTE. — A08: Aoki et al. (2008); B10: Behara et al. (2010); A11: Aoki et al. (2011, in prep.). Note that the stars SDSS J012617.9+060724.8 and SDSS J081754.9+264103.8 were reported on by both A08 and A11; the stars SDSS J091243.7+021623.7 and SDSS J134913.5-022942.8 were reported on by both B10 and A11.

<sup>a</sup> This star is a member of the calibration star sample analyzed in this paper.



TABLE 2  
NUMBERS OF STARS WITH DETECTED AND UNDETECTED  
CH G-BANDS AND FRACTIONS OF CARBON-RICH STARS  
AS A FUNCTION OF METALLICITY

Metallicity	$N_{C-norm}^D$	$N_{C-rich}^D$	$N_{C-norm}^L$	$N_{C-un}^L$	$F_{C-rich}$ %
$-1.5 < [Fe/H] \leq -1.0$	9113	149	335	3	1.6
$-2.0 < [Fe/H] \leq -1.5$	4376	377	2651	226	5.1
$-2.5 < [Fe/H] \leq -2.0$	506	173	1387	458	8.4
$-4.0 < [Fe/H] \leq -2.5$	13	46	201	201	18.0

NOTE. — *C-un* indicates stars with unknown carbon status (see text). Unlike the rest of the samples discussed in this paper, this table includes numbers without regard as to whether they have acceptable measured proper motions and radial velocities.

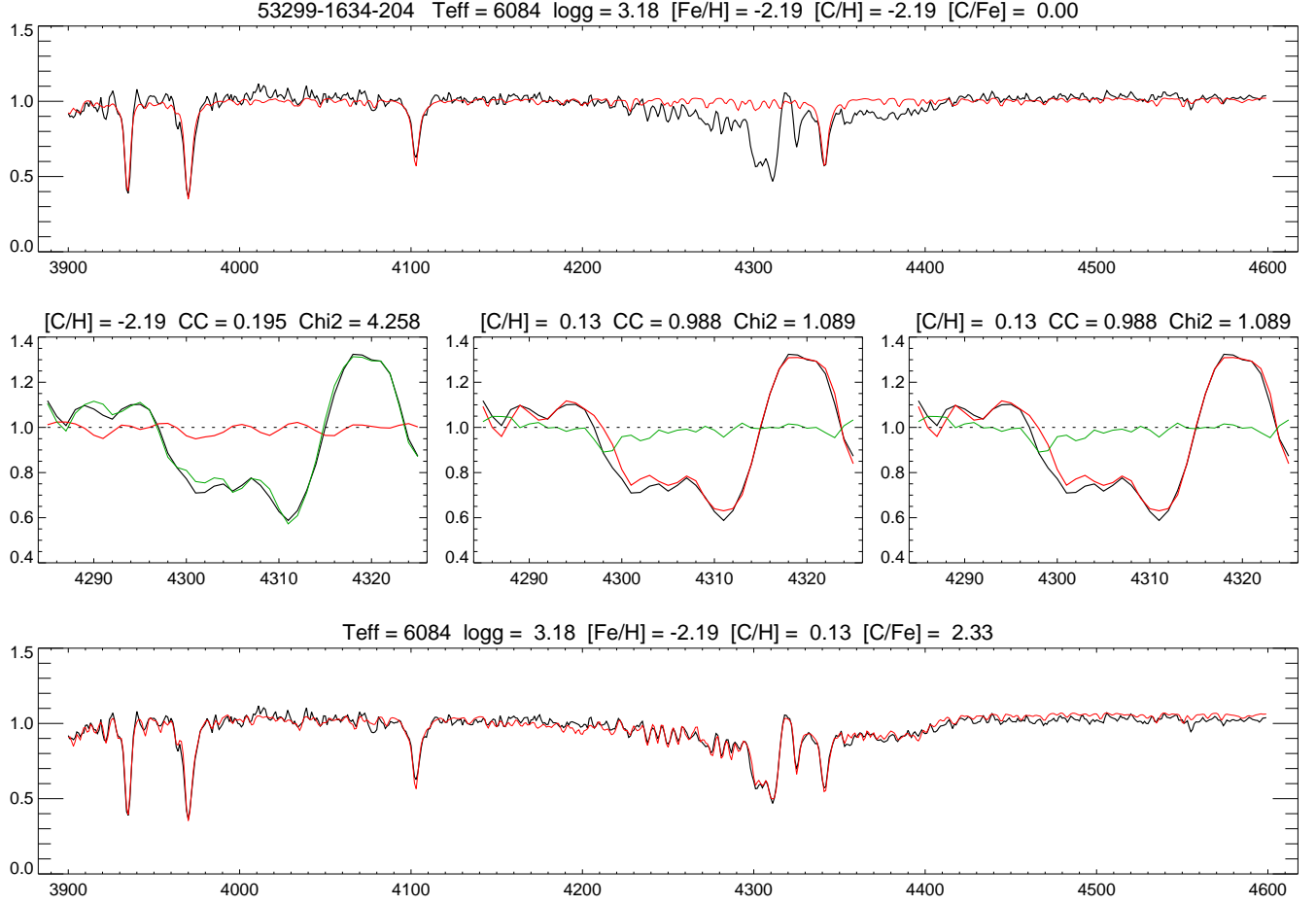


FIG. 1.— Example of the carbon-to-iron abundance estimation procedure. Upper panel: Input optical spectrum (black line) superposed with a synthetic spectrum (red line) with  $[\text{C}/\text{Fe}] = 0$  (the starting value). The legend at the top of this panel lists the input values determined by the SSPP for  $T_{\text{eff}}$ ,  $\log g$ , and  $[\text{Fe}/\text{H}]$ . Middle panels: Best matches to the CH G-band obtained from the three different search ranges considered (left:  $[\text{C}/\text{Fe}] < 0$ ; center:  $[\text{C}/\text{Fe}]$  covering the full grid range; right:  $[\text{C}/\text{Fe}] > 0$ ). The red line in each case is the best match; the green line is the ratio of the best match to the input spectrum. The legend above each of these panels provides the best estimate of  $[\text{C}/\text{H}]$ , along with a correlation coefficient between the synthetic spectrum and the input spectrum (CC), and the reduced  $\chi^2$  of the fit (Chi2). Note in the left-hand panel that no value of  $[\text{C}/\text{Fe}] < 0$  provides an acceptable match. The center and right-hand panels shown are identical, because the routine converged to the same value for the full grid search and the search restricted to  $[\text{C}/\text{Fe}] > 0$ . Lower panel: Final adopted match, represented by the superposed red line. The legend above this panel lists the resulting derived  $[\text{C}/\text{Fe}]$ .

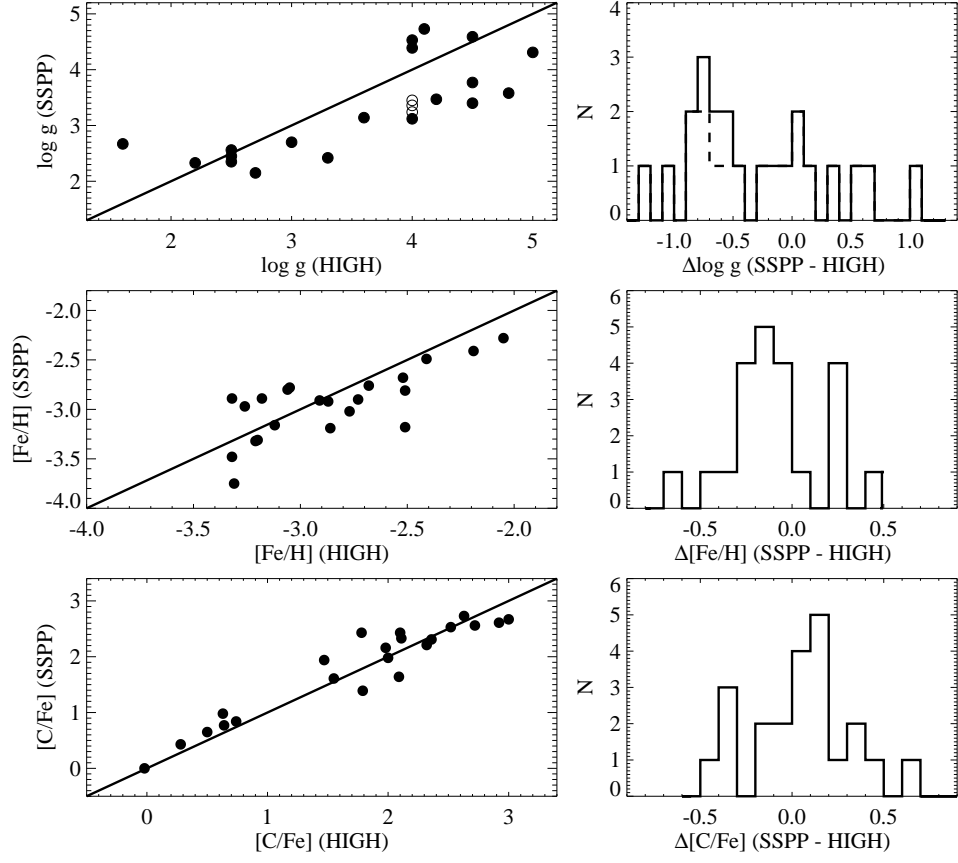


FIG. 2.— Left panels: Comparison of the estimates of atmospheric parameters ( $\log g$ ,  $[\text{Fe}/\text{H}]$ , and carbonicity,  $[\text{C}/\text{Fe}]$ , as derived from the low-resolution spectra (SSPP) and the high-resolution follow-up spectra (HIGH). A one-to-one line is shown for each. The open circles correspond to the stars with  $\log g$  values that were assigned, rather than derived (see text). Right panels: Histograms of the differences between the SSPP and HIGH determinations. The dashed bins indicate the stars with  $\log g$  values that were assigned, rather than derived. No comparison is made for the  $T_{\text{eff}}$  determinations, as the high-resolution estimates for the majority of our comparison sample were taken directly from the SSPP estimates (see text). Also see text for discussion of the reason for the apparently large dispersion in determination of  $\log g$ .



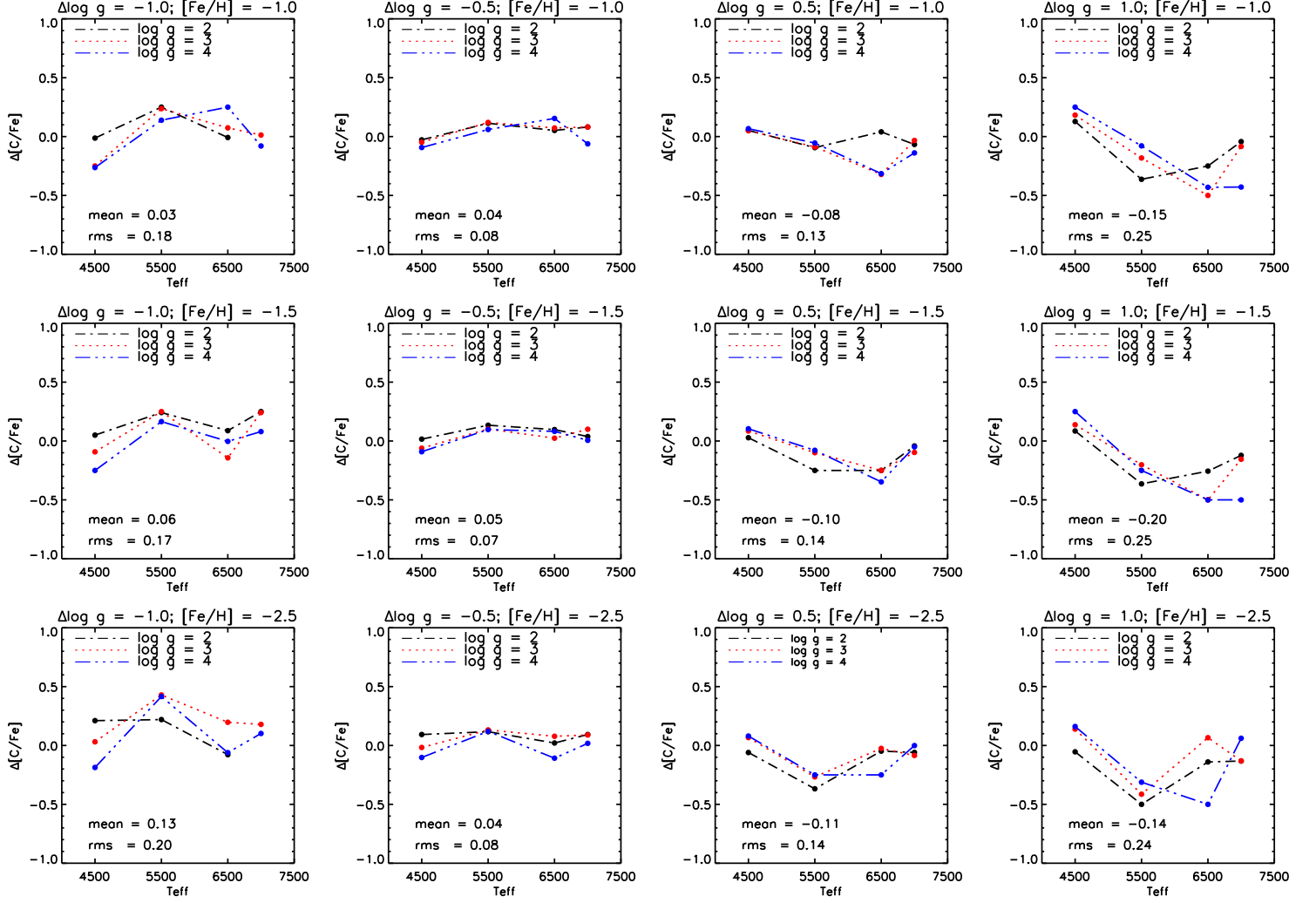


FIG. 3.— Results of an experiment to estimate the impact of incorrect  $\log g$  estimates on the derivation of  $[C/Fe]$  (plotted as  $\Delta[C/Fe]$ ), as described in the text. The top row of panels correspond to synthetic spectra with  $[Fe/H] = -1.0$ , the middle panels to  $[Fe/H] = -1.5$ , and the bottom panels to  $[Fe/H] = -2.5$ . From left to right, the columns of panels correspond to input perturbations in  $\log g$  of -1.0 dex, -0.5 dex, +0.5 dex, and +1.0 dex, respectively. The colored dots and lines shown in each panel correspond to input surface gravities (prior to perturbing their values) of  $\log g = 2.0$ , 3.0, and 4.0. The mean zero-point offsets and rms variations in the derived  $[C/Fe]$ , relative to the known value across all  $T_{\text{eff}}$  and  $\log g$  considered, are shown for each panel. The case illustrated here is for  $[C/Fe] = 0.0$ ; similar results pertain to the case  $[C/Fe] = +1.5$ .

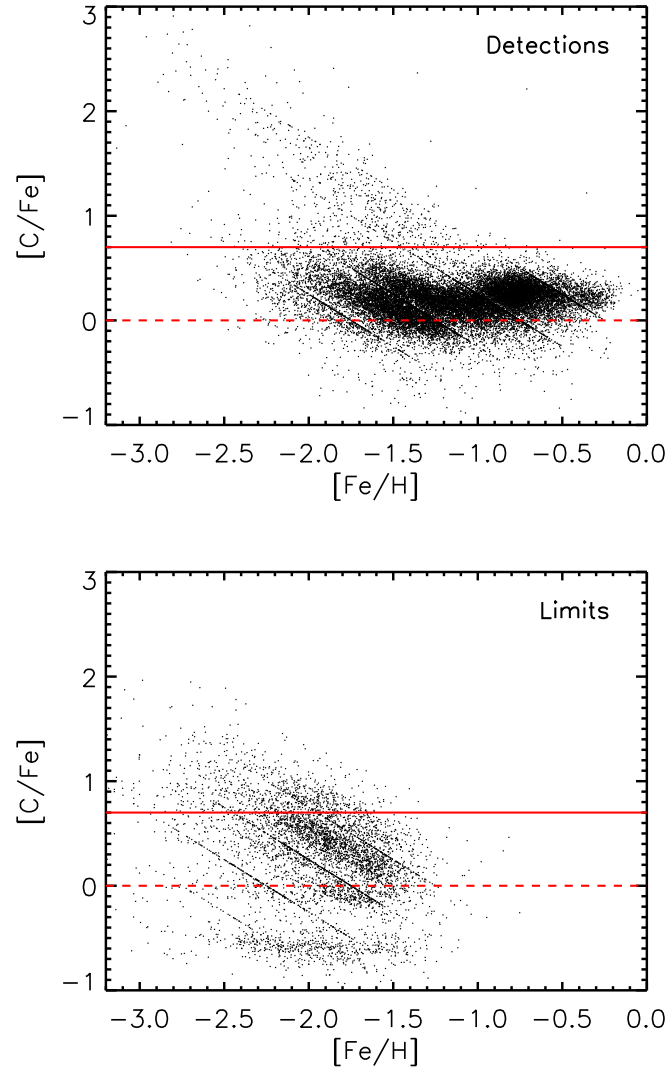


FIG. 4.— Carbonicity,  $[C/Fe]$ , as a function of metallicity,  $[Fe/H]$ , for subsample D (top panel) and subsample L (bottom panel). The dashed red line represents the solar carbon abundance ratio  $[C/Fe] = 0.0$ ; the solid red line denotes the adopted limit that divides C-norm stars from C-rich stars,  $[C/Fe] = +0.7$ . The “ridge lines” in both of these plots are due to grid effects in the chi-square fitting procedure.

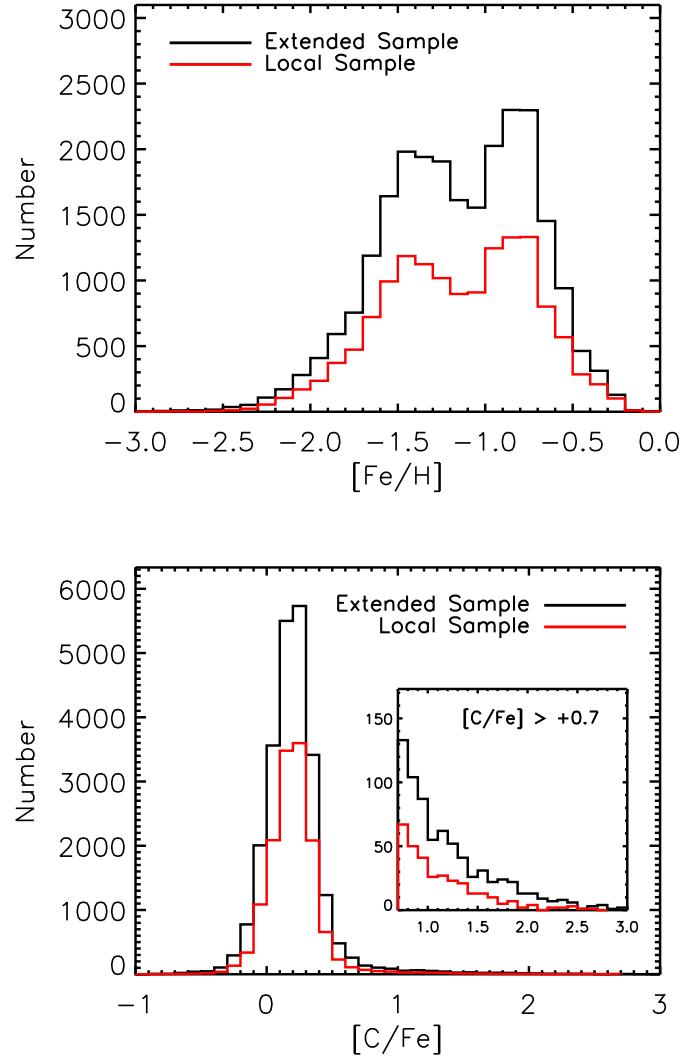


FIG. 5.— Upper panel: As-observed metallicity distribution function (MDF) for the Extended Sample of SDSS/SEGUE calibration stars (black histogram;  $d < 10$  kpc, no restriction on  $R$ ), and for the Local Sample (red histogram;  $d < 4$  kpc;  $7 \text{ kpc} < R < 10$  kpc). Lower panel: As-observed carbonicity distribution function (CarDF) for the Extended Sample of calibration stars (black histogram), and for the Local Sample (red histogram). Note that the Extended Sample contains significant numbers of dwarfs, main-sequence turnoff stars, and subgiants/giants (77%, 13%, and 10%, respectively), while the Local Sample primarily comprises dwarfs (88%) and main-sequence turnoff stars (9%), due to the larger volume explored by the subgiants and giants. The inset shows a rescaled view of the high-carbonicity tail. For both panels, only stars with carbon detections are used.



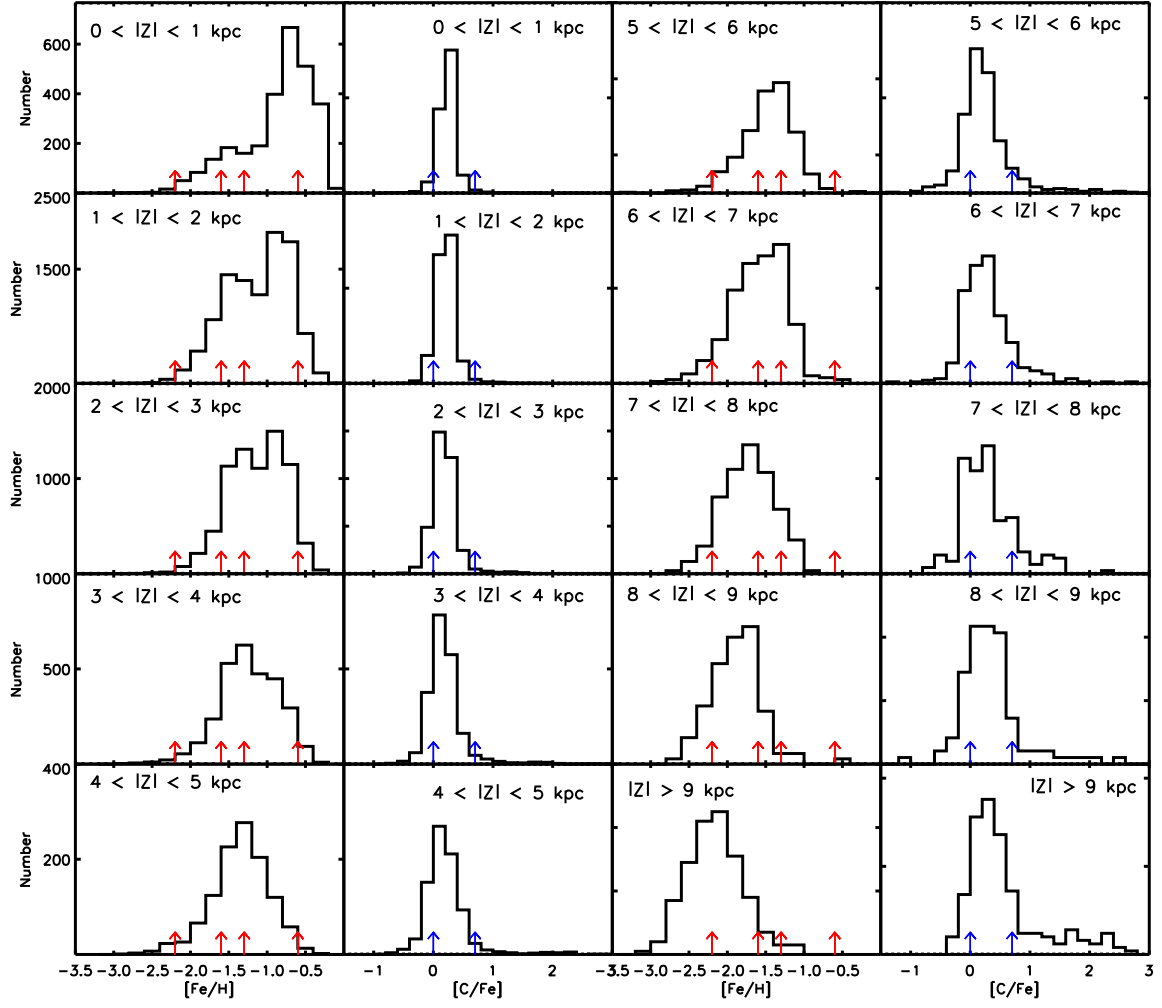


FIG. 6.— First and third columns: As-observed metallicity distribution functions (MDFs), for the Extended Sample of SDSS/SEGUE DR7 calibration stars, as a function of vertical distance from the Galactic plane. The histograms represent the MDFs obtained at different cuts of  $|Z|$ . The red arrows indicate the locations of the metallicity peaks of the MDF for the thick disk ( $-0.6$ ), the MWTD ( $\sim -1.3$ ), the inner halo ( $-1.6$ ), and the outer halo ( $-2.2$ ), respectively, assigned by C10. Second and fourth columns: As-observed carbonicity distribution functions (CarDFs), for the Extended Sample of SDSS/SEGUE DR7 calibration stars, as a function of vertical distance from the Galactic plane. The blue arrows show the location of the solar carbon-to-iron ratio ( $[C/Fe] = 0.0$ ), and the natural threshold that divides carbon-normal from carbon-rich stars ( $[C/Fe] = +0.7$ ). The histograms represent the CarDFs obtained at different cuts of  $|Z|$ . For all panels, only stars with carbon detections are used.

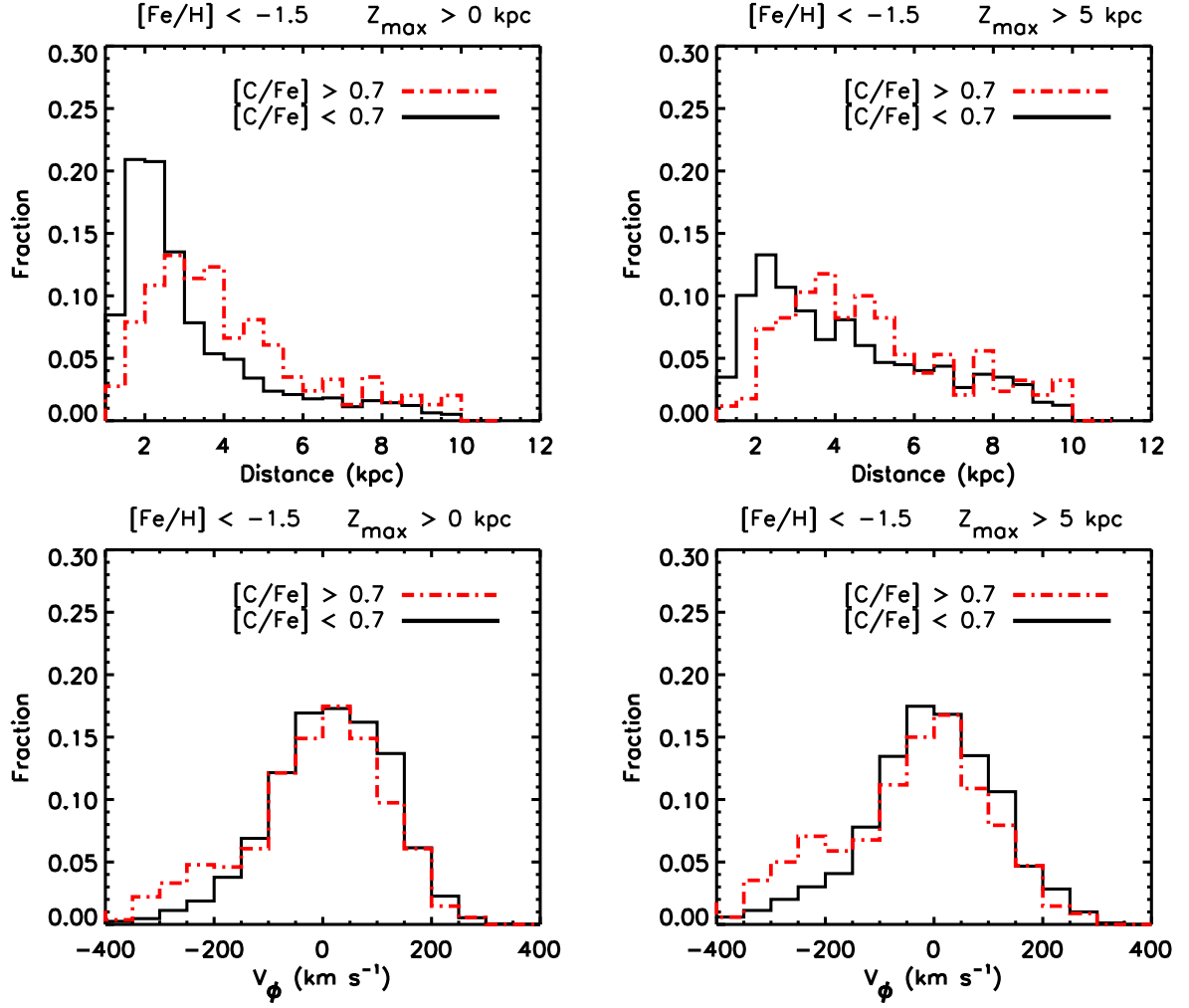


FIG. 7.— Distributions of estimated distances (top panels) and rotational velocity,  $V_\phi$  (bottom panels), for stars considered CEMP ( $[\text{C}/\text{Fe}] > +0.7$ ; dot-dashed red histograms), and non-CEMP ( $[\text{C}/\text{Fe}] < +0.7$ ; solid black histograms), for two cuts on  $Z_{\text{max}}$ . The stars are selected from the Extended Sample with  $[\text{Fe}/\text{H}] < -1.5$ . The left-hand column of panels includes stars at all  $Z_{\text{max}}$ ; the right-hand column of panels is only for stars satisfying  $Z_{\text{max}} > 5$  kpc. For all panels, only stars with carbon detections are used.

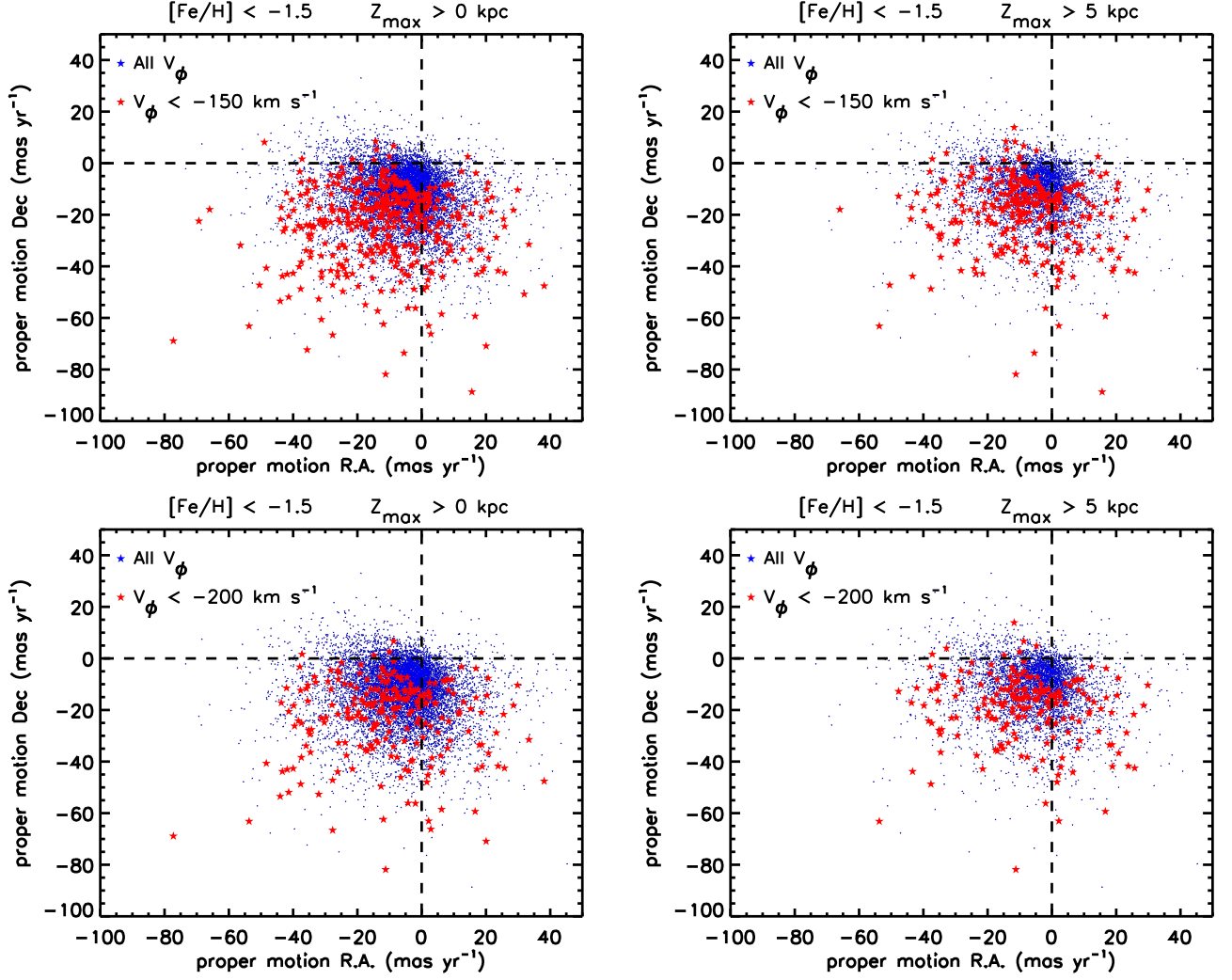


FIG. 8.— Measured proper motion components for stars in the Extended Sample with  $[\text{Fe}/\text{H}] < -1.5$  and two different cuts on  $Z_{\text{max}}$ . The left-hand column of panels includes stars at all  $Z_{\text{max}}$ ; the right-hand column of panels is only for stars satisfying  $Z_{\text{max}} > 5 \text{ kpc}$ . The small blue dots represent the entire sample satisfying these cuts; the filled red stars represent stars belonging to the highly retrograde tails shown in the bottom panels of Figure 7. The upper panels correspond to the sample of retrograde stars with  $V_\phi < -150 \text{ km s}^{-1}$ ; the lower panels correspond to the sample of retrograde stars with  $V_\phi < -200 \text{ km s}^{-1}$ . Clear differences in the distributions of proper motions exist between the stars in the highly retrograde tail and the rest of the sample. The dashed lines provide a zero proper motion reference frame. For all panels, only stars with carbon detections are used.



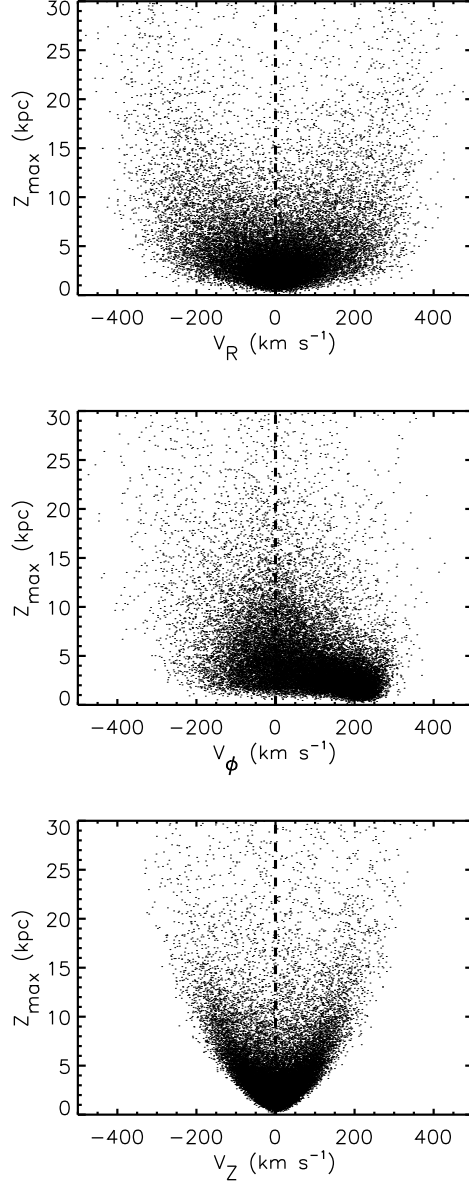


FIG. 9.— The relationship between  $Z_{\text{max}}$  and the cylindrical velocity components ( $V_R, V_\phi, V_Z$ ) for the SDSS/SEGUE calibration stars in the Extended Sample. The strong correlation between  $Z_{\text{max}}$  and the radial velocity component shown in the upper panel,  $V_R$ , as well as with the vertical velocity component shown in the lower panel,  $V_Z$ , is confirmed for the Extended Sample. The middle panel exhibits no strong correlation between  $Z_{\text{max}}$  and the rotational velocity component,  $V_\phi$ , other than that expected from the presence of the thick-disk and halo populations. The dashed line is a reference line at zero velocity for each component. Note, in the middle panel, the clear excess of stars with retrograde motions for  $Z_{\text{max}} > 10$ -15 kpc, which we associate with the outer-halo component. The panels include all stars, regardless of their carbon status.

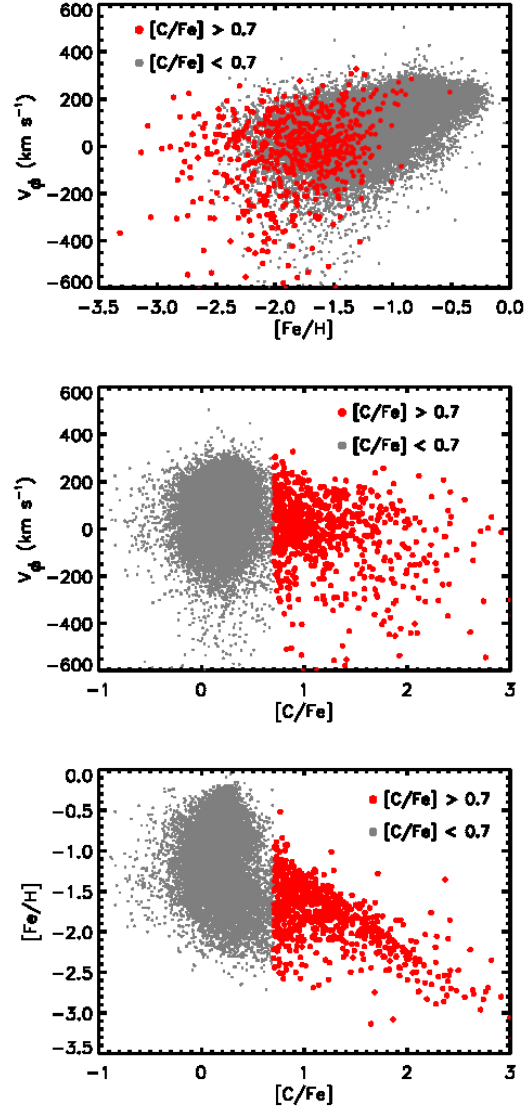


FIG. 10.— Global behavior of the basic parameters,  $V_\phi$ ,  $[Fe/H]$ , and  $[C/Fe]$ , for the Extended Sample of SDSS/SEGUE calibration stars with detected CH G-bands. Upper panel: Galactocentric rotational velocity as a function of the metallicity. Middle panel: Galactocentric rotational velocity as a function of  $[C/Fe]$ . Lower panel: Metallicity vs. carbonicity,  $[C/Fe]$ . In all panels, the gray dots represent stars with low carbonicity,  $[C/Fe] < +0.7$ ; the red dots denote the stars with high carbonicity,  $[C/Fe] > +0.7$ .

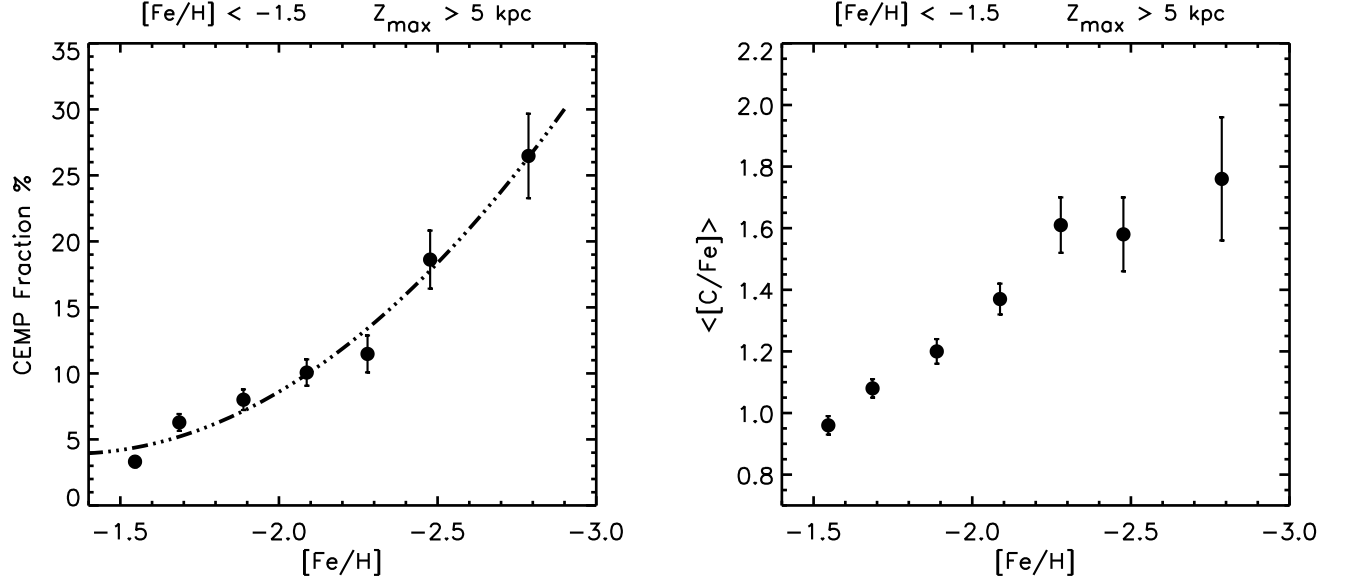


FIG. 11.— Left panel: Global trend of the CEMP fraction, as a function of  $[\text{Fe}/\text{H}]$ , for the low-metallicity stars of the Extended Sample with  $Z_{\text{max}} > 5 \text{ kpc}$ . Each bin of metallicity has width  $\Delta[\text{Fe}/\text{H}] = 0.2 \text{ dex}$ , with the exception of the lowest-metallicity bin, which includes all stars with  $[\text{Fe}/\text{H}] < -2.6$ . The error bars are evaluated with the jackknife method. The calculation of CEMP star frequency is made using Eqn. 2, which includes all stars of known carbon status, including the L subsample. A second-order polynomial fit to the observed distribution is shown by the dot-dashed line. Right panel: Global trend of the mean carbonicity,  $\langle [\text{C}/\text{Fe}] \rangle$ , as a function of  $[\text{Fe}/\text{H}]$ . Only those stars with detected CH G-bands are used. The bins are the same as used in the left panel. Errors are the standard error in the mean.



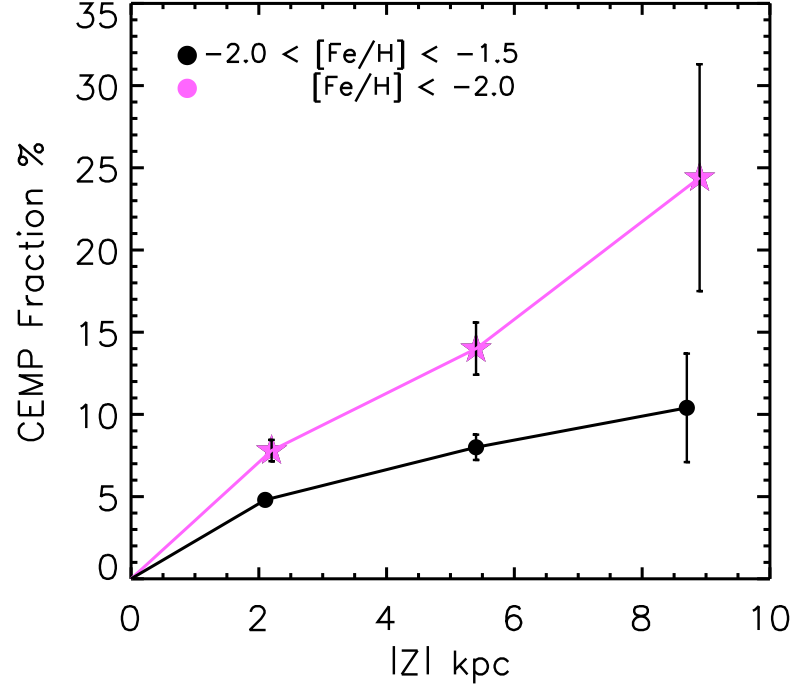


FIG. 12.— Global trend of the CEMP star fraction, as a function of vertical distance from the Galactic plane,  $|Z|$ , for the low-metallicity stars of the Extended Sample. The stars with  $-2.0 < [Fe/H] < -1.5$  are shown as filled black circles; those with  $[Fe/H] < -2.0$  are shown as magenta stars. Each bin has a width of  $\Delta|Z| = 4$  kpc, with the exception of the last bin, which cuts off at 10 kpc, the limiting distance of the Extended Sample. Errors are derived using the jackknife approach. The calculation of CEMP star frequency is made using Eqn. 2, which includes all stars of known carbon status, including the L subsample. Note the clear dependence of CEMP fraction on height above the Galactic plane, for both metallicity regimes.

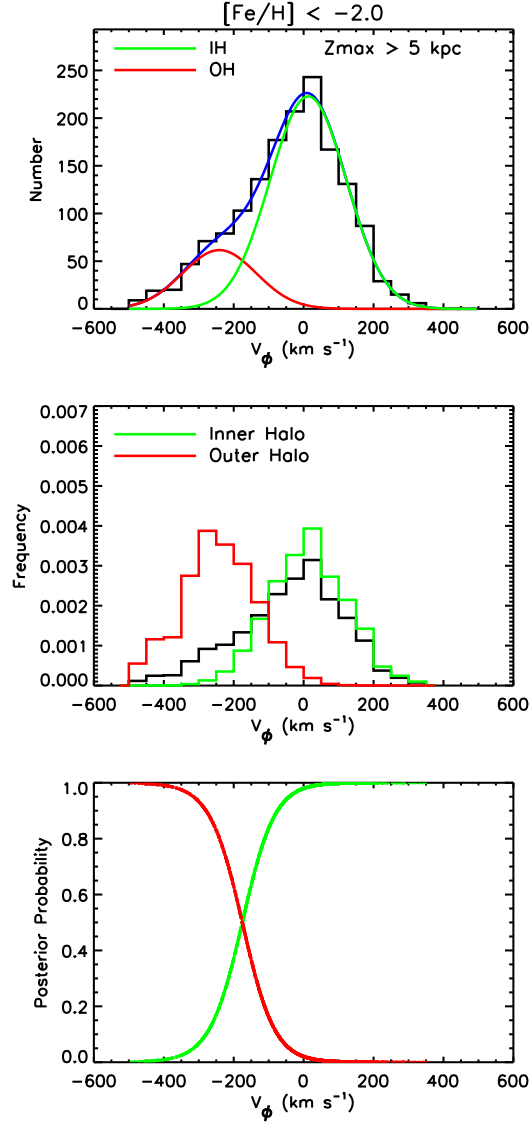


FIG. 13.— Rotational properties for the Extended Sample of SDSS/SEGUE DR7 calibration stars with metallicity  $[\text{Fe}/\text{H}] < -2.0$  and  $Z_{\text{max}} > 5$  kpc. Upper panel: The black histogram represents the observed distribution of  $V_\phi$ ; the green (inner halo), and red (outer halo) curves show the results of the Extreme Deconvolution analysis. Middle panel: The observed velocity distribution function (black histogram), and the inner- and outer-halo weighted velocity distribution functions (frequencies), denoted by the green and the red histograms, respectively. In this panel, all the distributions are normalized and take into account the membership probability of each star. Lower panel: The posterior probability for the inner- and outer-halo components as a function of the rotational velocity,  $V_\phi$ . Note that these plots use all stars in the Extended Sample satisfying the stated cuts, regardless of whether or not they have detected CH G-bands.

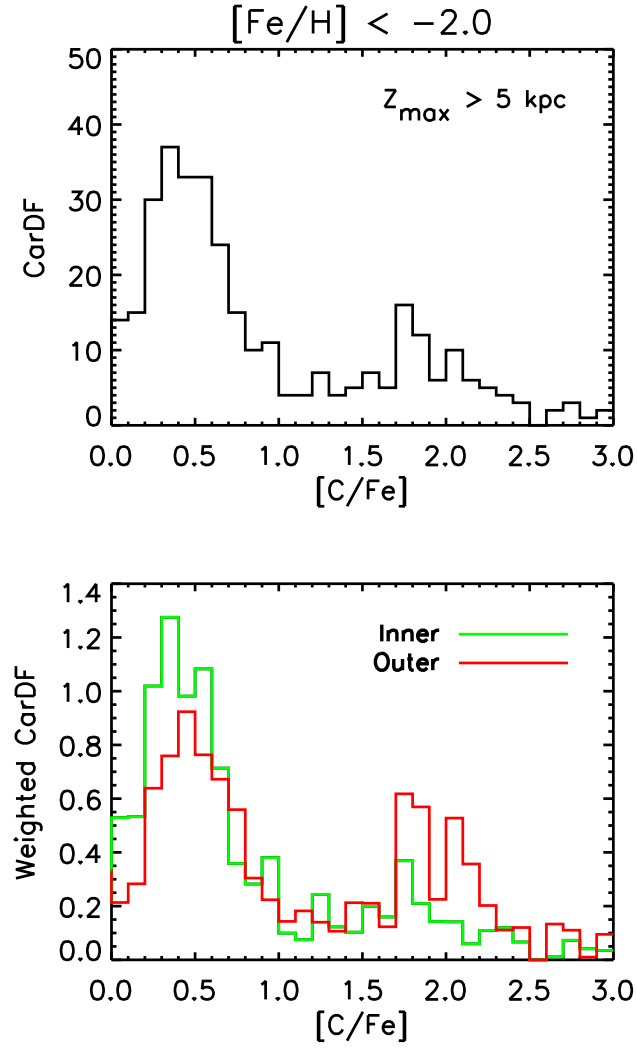


FIG. 14.— The carbonicity distribution functions (CarDF) for the Extended Sample with  $[Fe/H] < -2.0$  and  $Z_{\max} > 5$  kpc and with detected CH G-bands. Top panel: CarDF for the entire sample. Bottom panel: Weighted CarDF for the inner- and outer-halo components, shown by the green and red histograms, respectively.

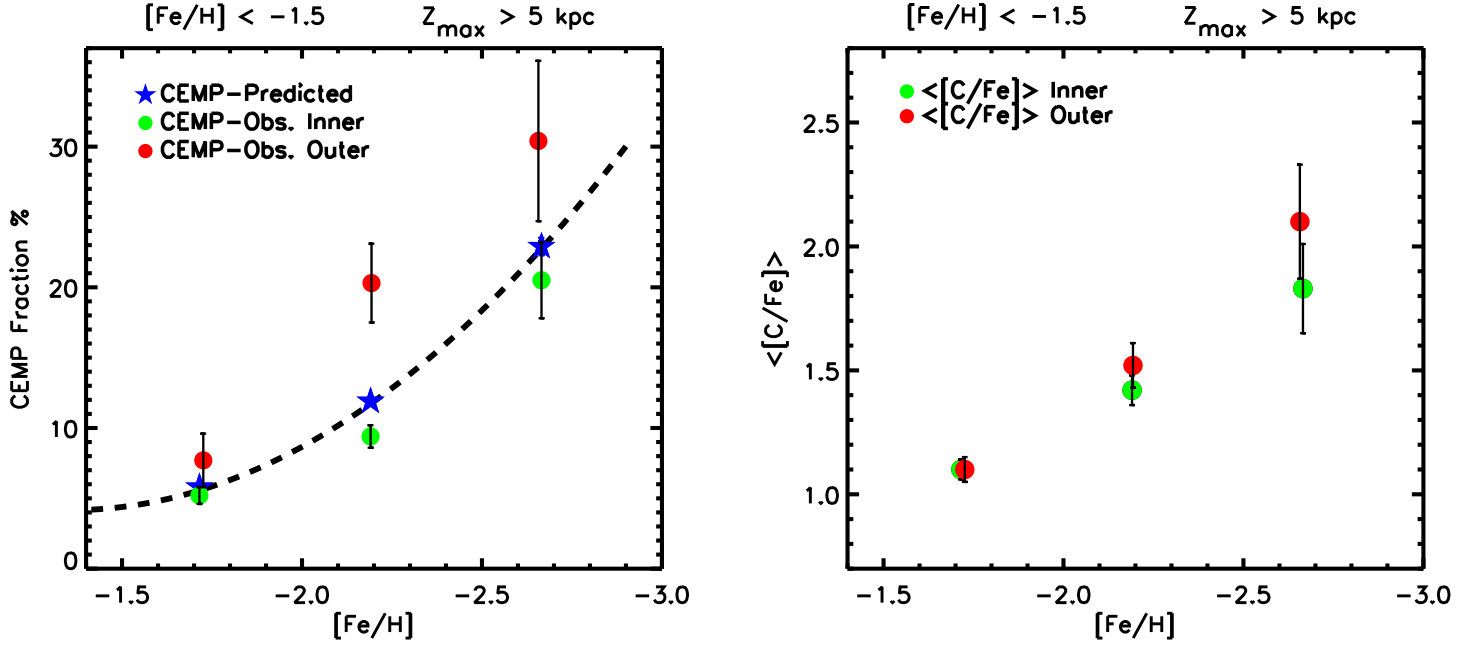


FIG. 15.— Left panel: Global trend of the CEMP star fraction as a function of  $[\text{Fe}/\text{H}]$  for the low-metallicity stars of the Extended Sample with  $Z_{\text{max}} > 5$  kpc. The dashed curve is a second-order polynomial fit representing the global trend. The blue filled stars represent the predicted values of the CEMP fractions in each bin of metallicity, having a width of  $\Delta[\text{Fe}/\text{H}] = 0.5$  dex. The green and red filled circles show the location of the observed CEMP star fractions for the inner halo and outer halo, respectively, based on the XD method with the hard-cut-in-probability approach (see text). The error bars are evaluated with the jackknife method. The calculation is made using Eqn. 2, which includes all stars of known carbon status, including the L subsample. Right panel: Global trend of the mean carbonicity,  $\langle[\text{C}/\text{Fe}]\rangle$ , as a function of  $[\text{Fe}/\text{H}]$ . Only those stars with detected CH G-bands are used. The green and red filled circles show the mean carbonicity for the inner halo and outer halo, respectively, based on the Extreme Deconvolution method with the hard-cut-in-probability approach (see text). The bins are the same as used in the left panel. Errors are the standard error in the mean. No significant difference is seen for the inner- and outer-halo subsamples.